

1 **Grain fragmentation and frictional melting during initial experimental**  
2 **deformation and implications for seismic slip at shallow depths**

3

4 Chien-Cheng Hung<sup>1#†</sup>, Li-Wei Kuo<sup>1\*#</sup>, Elena Spagnuolo<sup>2</sup>, Chun-Chieh Wang<sup>3</sup>, Giulio  
5 Di Toro<sup>2,4</sup>, Wen-Jie Wu<sup>1</sup>, Jia-Jyun Dong<sup>5</sup>, Wayne Lin<sup>6</sup>, Hwo-Shuenn Sheu<sup>3</sup>, En-Chao  
6 Yeh<sup>7</sup>, Pei-Shan Hsieh<sup>6</sup>

7

8 <sup>1</sup>Department of Earth Sciences, National Central University, Taoyuan, Taiwan

9 <sup>2</sup>Istituto Nazionale di Geofisica e Vulcanologia, Rome, Italy

10 <sup>3</sup>National Synchrotron Radiation Research Center, Hsinchu, Taiwan

11 <sup>4</sup>Dipartimento di Geoscienze, Università di Padova, Padua, Italy

12 <sup>5</sup>Graduate Institute of Applied Geology, National Central University, Taoyuan, Taiwan

13 <sup>6</sup>Industrial Technology Research Institute, Hsinchu, Taiwan

14 <sup>7</sup>Department of Earth Sciences, National Taiwan Normal University, Taipei, Taiwan

15

16 \*corresponding author

17 Address: No. 300, JhongDa Rd., Jhongli District, Taoyuan City 32001, Taiwan

18 Tel: +886-3-4227151 ext:65628 Fax: +886-3-4222044

19 E-mail: liweikuo@ncu.edu.tw; liweikuo@gmail.com

20

21 † now at Earth Simulation Laboratory, Department of Earth Sciences, Utrecht

22 University, Utrecht, The Netherlands

23 # equal contribution

24

25 **Abstract**

26 During seismic slip, the elastic strain energy released by the wall rocks drives grain  
27 fragmentation and flash heating in the slipping zone, resulting in formation of  
28 (nano)powders and melt droplets, which lower the fault resistance. With progressive  
29 seismic slip, the frictional melt covers the slip surface and behaves as a lubricant  
30 reducing the coseismic fault strength. However, the processes associated to the  
31 transition from grain fragmentation to bulk frictional melting remain poorly  
32 understood. Here we discuss *in-situ* micro-analytical investigations performed on  
33 experimentally produced solidified frictional melts from the transition regime  
34 between grain fragmentation and frictional melting. The experiments were performed  
35 on granitic gneiss at seismic slip rates (1.3 and 5 m/s), normal stresses ranging from 3  
36 to 30 MPa. At normal stresses < 12 MPa, the apparent friction coefficient  $\mu_{app}$  (shear  
37 stress vs. normal stress) evolves in a complex manner with slip:  $\mu_{app}$  decreases  
38 because of flash weakening, increases up to a peak value  $\mu_{p1} \sim 0.6-1.0$ , slightly  
39 decreases and increases again to a second peak value  $\mu_{p2} \sim 0.44-0.83$ , and eventually  
40 decreases with displacement to a steady-state value  $\mu_{ss} \sim 0.3-0.45$ . *In-situ* synchrotron  
41 observations of the solidified frictional melt show abundance of ultra-fine quartz  
42 grains before  $\mu_{p2}$  and enrichment in  $\text{SiO}_2$  at  $\mu_{p2}$ . Because partial melting occurs on the  
43 ultra-fine quartz grains and, as a consequence, it suggested that the second  
44 re-strengthening ( $\mu_{p2}$ ) is induced by the higher viscosity of the melt due to its  
45 enrichment in Si from melting of the ultra-fine quartz grains derived from grain  
46 fragmentation.

47

48 Keyword: frictional melting, grain fragmentation, ultrafine quartz, viscosity,  
49 synchrotron analysis.

## 50 **1. Introduction**

51 Numerous physical and chemical processes have been theoretically and  
52 experimentally proposed to justify fault lubrication during seismic slip, for example,  
53 flash heating (Rice, 2006; Beeler et al., 2008; Goldsby and Tullis, 2011), powder  
54 lubrication (Han et al., 2010; Reches and Lockner, 2010), frictional melting (Spray,  
55 2005; Di Toro et al., 2006a), silica gel formation (Di Toro et al., 2004),  
56 elastohydrodynamic lubrication (Brodsky and Kanamori, 2001; Cornelio et al., 2019),  
57 grain size- and temperature-dependent processes (Green et al., 2015; De Paola et al.,  
58 2015; Spagnuolo et al., 2015; Rowe et al., 2019) and thermal decomposition (Han et  
59 al., 2007; Collettini et al., 2013). In particular, on a fault patch in silicate-built rocks,  
60 flash heating and melting (Goldsby and Tullis, 2011) or grain fragmentation of the  
61 rock (Green et al., 2015; De Paola et al., 2015; Spagnuolo et al., 2015; Rowe et al.,  
62 2019; Chen et al., 2017a) may occur during the initial stages of seismic slip at the  
63 passage of the earthquake rupture propagation front. With progressive slip, the  
64 continuously generated melt droplets can accumulate to form a continuous melt layer  
65 possibly resulting in melt lubrication (Spray, 1995; Hirose and Shimamoto, 2005).  
66 Therefore, studies on powder generation, flash heating and melting, and the formation  
67 of a continuous melt layer provided criteria for understanding fault lubrication  
68 (Reches and Lockner, 2010; Chen et al., 2017a; Spray, 1995; 2005; Di Toro et al.,  
69 2006; Rice, 2006; Beeler et al., 2008; Goldsby and Tullis, 2011).

70 However, the transition between fault rock comminution and frictional melting  
71 remains unclear. More relevantly, how do the associated frictional properties derived  
72 from both fault comminution and frictional melting affect the fault strength during  
73 fault rupture is not well-constrained. Here, we address these questions by conducting  
74 rock friction experiments on granitic gneiss at seismic rates and further discuss how  
75 the presence of fragmented grains and the chemical evolution of the friction melt  
76 influence the frictional behavior of the experimental fault.

77

## 78 **2. Materials and Methods**

### 79 **2.1 Starting materials**

80 The exhumed pseudotachylyte-bearing fault, which crosscuts the granitic gneiss  
81 of the Tananao Metamorphic Complex (TMC), crops out in the Hoping area, northeast  
82 Taiwan (Chu et al., 2012; Fig. 1a). The fault zone rocks are mainly cataclasites and  
83 mylonites overprinted by pseudotachylytes. Pseudotachylytes were generated at  
84 depths > 4 km about 1.6 Ma ago (Chen et al., 2017) in faults accommodating  
85 displacements by up to 220 mm (corresponding to earthquakes of  $M_W 6.4 \pm 0.4$  if all  
86 the displacement would be associated to a single seismic slip event; Korren et al.,  
87 2015). Pseudotachylytes form vein and injection veins networks that intrude the host

88 granitic gneiss, and they were used to infer earthquake source parameters (e.g., slip  
 89 vectors, Korren et al., 2015; brushlines, Ferré et al., 2016). We used the granitic gneiss  
 90 from the Hopping borehole cores drilled by the Industrial Technology Research  
 91 Institute (ITRI) as the starting materials for the rotary shear experiments (Fig. 1b and  
 92 1c). The mineral composition of the core granitic gneiss is 35–40% quartz, 15–25%  
 93 feldspar, 20–25% micas (muscovite dominant) and 5–10% other accessory minerals  
 94 (estimated by optical microscope analysis of thin sections). This estimated  
 95 composition is similar to the modal content of the granitic gneiss cropping out in the  
 96 area with 30–35% quartz, 20–25% feldspar, 30–35% micas (both muscovite and  
 97 biotite), 3–5% clinozoisite-epidote and titanite, as well as 2% of other accessory  
 98 minerals (Chu et al., 2012). The bulk chemical composition of the granitic gneiss is  
 99 also shown in Table 1. The granitic gneiss has a heterogeneous mineralogical  
 100 distribution due to the presence of a foliation enriched in muscovite or in quartz and  
 101 feldspar (Fig. 1b and 1c). To achieve more homogenous mineralogy of the sliding  
 102 surface, the samples prepared for the experiments were drilled with the long axis  
 103 oblique (approximately 25° to 30°) to the gneissic foliation.

104

## 105 **2.2 Rock deformation experiments**

106 Rock deformation experiments were conducted with the low-to-high velocity  
 107 rotary shear friction apparatus (LHVR) installed at the National Central University  
 108 (NCU), Taiwan (Yang et al., 2014; Kuo et al., 2015), and the slow-to-high velocity  
 109 apparatus (SHIVA) at the Istituto Nazionale di Geofisica e Vulcanologia (INGV,  
 110 Rome), Italy (Di Toro et al., 2010). The latter was used to extend the applied normal  
 111 stresses up to 30 MPa and perform an experiment under vacuum conditions.

112 For LHVR, the samples were solid cylinders (25 mm external diameter) which  
 113 were tightly confined with iron wires (Fig. 1b). For SHIVA, the samples were hollow  
 114 cylinders (50 mm external, 30 mm internal diameters) which were jacketed with an  
 115 external aluminum ring (Fig. 1c; Niemeijer et al., 2011; Nielsen et al., 2012). To  
 116 improve the alignment of two mounted samples before the experiments, for LHVR,  
 117 we gently knocked the edge of the upper one until the measured un-centered degree  
 118 was lower than 10 μm, and, for SHIVA, we pre-ground the slip surface of the samples  
 119 at 1 cm/s and 1 MPa (Niemeijer et al., 2011). The pre-grinding lasted until the  
 120 recorded torque achieved a constant value which is associated with the parallelism of  
 121 the two opposite sliding surfaces.

122 Because of the rotary configuration of the two machines used, both slip and slip  
 123 rate increase with sample radius. As a consequence, we define the equivalent slip rate  
 124  $V_e$  (Shimamoto and Tsutsumi, 1994; Hirose and Shimamoto, 2005):

$$125 \quad V_e = \frac{4\pi R(r_{ext}^2 + r_{ext}r_{int} + r_{ext}^2)}{3(r_{ext} + r_{int})} \left[ \frac{m}{s} \right] \quad \text{Eq. 1}$$

126 where  $R$  is the revolution rate of the motor (i.e., the target  $R$  in the experiments  
 127 presented here were 1500 rpm for LHVR and 3000 rpm for SHIVA),  $r_{\text{ext}}$  the external  
 128 radius (12.5 and 25 mm for LHVR and SHIVA, respectively), and  $r_{\text{int}}$  the internal  
 129 radius (0 mm and 15 mm for LHVR and SHIVA, respectively) of the samples (Fig. 1).  
 130 The experimental conditions above resulted in target  $V_e$  of 1.3 m/s and 5 m/s for  
 131 LHVR and SHIVA, respectively. Hereafter we refer to the "equivalent slip rate" as  
 132 slip rate. The measured torque ( $T$ ) allows us to determine the shear stress ( $\tau$ ) by  
 133 assuming that  $\tau$  is constant over the entire slip surface (Hirose and Shimamoto, 2005):

$$134 \quad T = \int_{r_{\text{int}}}^{r_{\text{ext}}} 2\pi r \tau r^2 dr = \frac{2\pi\tau}{3} (r_{\text{ext}}^3 - r_{\text{int}}^3) \text{ [N m]} \quad \text{Eq. 2}$$

135 Given the strong assumption of a constant shear stress over the entire slip surface,  
 136 which cannot be the case as the shear stress varies with slip rate (e.g., Di Toro et al.,  
 137 2011) and in the cylindrical configuration the slip rate increases with the sample  
 138 radius, mechanical data obtained with hollow cylinders are more accurate than those  
 139 obtained with solid cylinders. From Eq. 2, the friction coefficient  $\mu$  is:

$$140 \quad \mu = \frac{\tau}{\sigma} = \frac{3T}{2\pi\sigma(r_{\text{ext}}^3 - r_{\text{int}}^3)} \quad \text{Eq. 3}$$

141 hereafter we refer to  $\mu$  as apparent friction coefficient  $\mu_{\text{app}}$  for the following  
 142 description.

143 The LHVR experiments were conducted at normal stresses of 3, 6, 9, 12, and 19  
 144 MPa, at a target slip rate of 1.3 m/s, and under room humidity conditions. The SHIVA  
 145 experiments were conducted at the normal stresses of 3 and 30 MPa, respectively, and  
 146 at a target slip rate of 5 m/s under both vacuum and room humidity conditions (Table  
 147 2). All mechanical data (torque, angular rotation, and axial displacement) were  
 148 acquired at a frequency up to 1 kHz and 25 kHz for LHVR and SHIVA, respectively.  
 149 The friction coefficient of the granitic gneiss evolved in a complex manner with slip.  
 150 Because of this, we conducted slip-stepping experiments or experiments that were  
 151 stopped at the about the maximum or minimum values of the friction coefficient.

152

### 153 **2.3 Analytical methods**

- 154 1. We impregnated the experimental products of LHVR with epoxy resin and  
 155 prepared petrographic thin sections and rock slices, both cut across the diameter  
 156 of the sample and perpendicular to slipping surface. The petrographic thin  
 157 sections were prepared with a thickness of 30  $\mu\text{m}$ , mounted on silica glass and  
 158 polished by 0.3  $\mu\text{m}$  thick alumina powder for optical and scanning electron  
 159 microscopy analysis. The thickness of rock slices were  $\sim 1$  mm for *in-situ*  
 160 synchrotron X-ray diffraction (XRD) and micro-Raman spectroscopy analysis.
- 161 2. Three-lens optical microscopy (OM) (Leica DMLP) coupled with an image

162 capture system, and field emission scanning electron microscopy, coupled with  
163 an energy dispersive spectrometer (FESEM/EDX) (JSM-7000F model) equipped  
164 at the National Central University, Taiwan, were used to investigate the  
165 microstructures and determine the semi-quantitative chemical composition of the  
166 solidified frictional melt. For SEM-EDX, the petrographic sections were  
167 sputtered with platinum at 5 nm thickness and semi-quantitatively analyzed at 15  
168 kV with a focused beam of  $\sim 1 \mu\text{m}$  in diameter.

169 3. The *in-situ* synchrotron XRD installed at the beamline BL01C2 in the National  
170 Synchrotron Radiation Research Center (NSRRC), Taiwan, was used to  
171 determine the mineral assemblages of both the solidified frictional melt and the  
172 host rock. The analyses were operated at a wavelength of  $0.774910 \text{ \AA}$ , with an  
173 electron beam energy of 1.5 GeV and a beam size of  $150 \mu\text{m}$  in diameter.  
174 Because of the presence of large grains ( $\sim 1.0 \text{ mm}$  in size) of quartz, the samples  
175 of gneiss, differently from the solidified frictional melts, were reduced into  
176 powders and analyzed. This prevented the presence of intensity anomalies in the  
177 XRD spectra due to the occurrence of crystals (e.g., quartz) larger than the X-ray  
178 beam (Kuo et al., 2014a, b). However, the intensity anomalies can still be  
179 observed in the results of the glass matrix owing to the presence of large survivor  
180 quartz or feldspar grains. To reduce the effect of intensity anomalies and  
181 representatively present the synchrotron XRD data, the spectra were reported as  
182 the average values of three analyses on the same sample.

183 4. The micro-Raman spectroscopy (Horiba Jobin Yvon UV-VIS Labram HR) at the  
184 National Taiwan Museum was used to determine the presence of water within the  
185 solidified frictional melt. We focused on the region from  $100$  to  $4,000 \text{ cm}^{-1}$  on  
186 the Raman spectrum. The analysis was operated with a  $532 \text{ nm}$  laser as an  
187 excitation source with a beam size of  $1\text{--}2 \mu\text{m}$  in diameter under a  $\times 100$  objective  
188 with a final laser power of  $100 \text{ mW}$  on the sample surface. A charged-coupled  
189 device (CCD) detector was installed in the microscope used to focus the  
190 excitation laser beam to collect the backscattered Raman signal. We collected  
191 three data of the matrix per deformed sample for the solidified frictional melt at  
192 an acquisition time of  $15 \text{ s}$  per analysis. We added the Raman spectra of pure  
193 water and quartz for comparison.

194 5. The synchrotron transmission X-ray microscopy (TXM) at the beamline BL01B1  
195 (Song et al., 2007a, b; Yin et al., 2006) at the NSRRC, Taiwan, was used to  
196 obtain X-ray radiographies to determine the particle size distribution (PSD) of  
197 the survivor clasts hosted in the solidified frictional melt. The analysis was  
198 conducted on a  $30\text{-}\mu\text{m}$ -thick sample collected from the petrographic thin sections

199 over an area of 375  $\mu\text{m}$  x 75  $\mu\text{m}$ . The beam X-ray energy was 8 keV and the  
200 analysis had a spatial resolution of 50-nm (see Song et al., 2007a, b).

201 6. The software *ImageJ* (available at <https://imagej.nih.gov/ij/>) was used to process  
202 the images of both the back scattering electron (BSE) and the TXM to estimate  
203 the PSD of the survivor grains within the solidified frictional melt. *ImageJ*  
204 allowed us to measure the size of quartz grains by exploiting the gray contrast  
205 between the glass matrix and the quartz grains in the BSE images (Kuo et al.,  
206 2015). On the contrary, we draw by hand the survivor grains from the TXM  
207 images due to the difficulty of the contrast identification between glass matrix  
208 and grains. By doing this, the overlapping of the survivor grains could be also  
209 clearly identified.

210 7. One experiment (LHVR1097) performed on granitic gneiss from the outcrop was  
211 recorded with an infrared thermal-sensing camera (thermoIMAGER TIM160,  
212 MICRO-EPSILON) to measure the temperature evolution of the experimental  
213 fault with slip. The infrared camera, integrated with the TIMConnect software,  
214 provided an instantaneous measurement of the temperature from 150°C to 900°C  
215 over an area of 0.6 mm in diameter at an acquisition rate of 10-500 Hz. Since the  
216 slipping zone is < 0.3 mm in thickness and the temperature is measured from  
217 outside, the measured temperatures yielded a minimum estimate of the  
218 temperatures achieved in the slipping zone.

219

### 220 3. Results

#### 221 3.1 Frictional behavior and temperature evolution during fast shear experiments

222 The mechanical data exhibit a complicated evolution of  $\mu_{\text{app}}$  with slip, which  
223 varied with normal stress (Fig. 2a). At slip initiation, once the static friction  $\mu_s$  was  
224 overcome,  $\mu_{\text{app}}$  decreased rapidly to a first minimum value (possibly associated with  
225 flash heating and weakening, see discussion). Then the frictional evolution varied  
226 with normal stress:

227 *At large normal stresses* ( $\geq 12$  MPa, e.g., experiment s1289, Fig. 2a)  $\mu_{\text{app}}$   
228 increased to a peak value  $\mu_{p1} = 0.66$  and then dramatically decreased to a low value of  
229  $0.16 \pm 0.01$  (an average value of friction coefficient after peak friction and before the  
230 sample was broken) defined in the literature as steady state friction  $\mu_{\text{ss}}$  (e.g., Di Toro  
231 et al., 2011). At the end of slip, during sample deceleration,  $\mu_{\text{app}}$  increased again. In  
232 general, this frictional evolution with slip is consistent with previous experiments  
233 performed on silicate-built cohesive rocks sheared at seismic slip rates (Hirose and  
234 Shimamoto, 2005; Di Toro et al., 2006a, b; Niemeijer et al., 2011; Passelègue et al.,  
235 2016).

236 *At low normal stresses* (< 12 MPa, e.g., experiments LHVR 0438 and

237 LHVR0452, Fig. 2a and 3), after slip initiation and initial flash weakening,  $\mu_{app}$  first  
238 increased to a peak value at  $\mu_{p1} \sim 1.0$ , then decreased to 0.8-0.5, then increased again to  
239 a second peak value at  $\mu_{p2} \sim 0.44-0.83$  and eventually decreased with displacement to  
240  $\mu_{ss} \sim 0.3 \pm 0.01-0.45 \pm 0.08$ . Then, similarly to the large normal stress experiments,  
241  $\mu_{app}$  increased again at the end of slip (Fig. 2a). This complicated evolution, though  
242 observed in previous experiments, has been only partly discussed (e.g., Hirose and  
243 Shimamoto, 2005; Di Toro et al., 2006).

244 With the aim of investigating the process responsible for the  $\mu_{p1}$  and  $\mu_{p2}$ , we  
245 analyzed the slipping zone produced in dedicated experiments stopped, with  
246 increasing slip (slip-stepping experiments, Fig. 3), after:

- 247 (1) 1.5 m of slip corresponding to  $\mu_{p1}$  (State A, experiment LHVR0487);
- 248 (2) 2.6 m of slip corresponding to the frictional strength decrease between  $\mu_{p1}$  and  $\mu_{p2}$   
249 (State B, experiment LHVR0534);
- 250 (3) 2.1 m of slip corresponding to ca.  $\mu_{p2}$  (State C, experiment LHVR0452);
- 251 (4) 5.7 m of slip during the final weakening (State D, "steady-state" conditions,  
252 experiment LHVR0438).

253 To illustrate the temperature evolution with slip for loading conditions identical  
254 to those imposed in the reference experiment LHVR0438 where "steady-state"  
255 conditions were achieved, experiment LHVR1097 was equipped with an infrared  
256 thermal-sensing camera. Because the emissivity  $\varepsilon$  of melt varies with temperature, we  
257 set two values of  $\varepsilon$ , 0.55 and 0.9 for high and low temperature, respectively (Abtahi et  
258 al., 2002). For  $\varepsilon = 0.55$ , the temperature of the slipping zone immediately increased to  
259  $\sim 430^\circ\text{C}$  (ca. 0.6 m of slip in Fig. 3e), slightly rose to  $\sim 500^\circ\text{C}$  at State A (ca. 1.2 m of  
260 slip), slightly decreased and remained a constant value of  $\sim 450^\circ\text{C}$  during State B  
261 (between 1.2 and 2 m of slip), steadily rose to  $\sim 750^\circ\text{C}$  at State C (between 2 and 3 m  
262 of slip), and eventually increased to a constant value of  $\sim 850^\circ\text{C}$  during State D (from  
263 3 m to the end of slip). There was a loss of temperature measurements (between  $\sim 3.5$   
264 to 4 m of slip) because of connection issues with the infrared camera. For  $\varepsilon = 0.9$ ,  
265 with respect to the estimated temperatures for  $\varepsilon = 0.55$ , temperatures achieved in the  
266 different States were lower by about  $\sim 100^\circ\text{C}$  for States A and B,  $\sim 200^\circ\text{C}$  for State C  
267 and  $\sim 250^\circ\text{C}$  for State D.

268 Regarding the entire experimental dataset, the initial peak (corresponding to  $\mu_{p1}$ )  
269 and steady-state (corresponding to  $\mu_{ss}$ ) shear stress increased linearly with normal  
270 stress, resulting in an effective friction coefficient of  $\sim 0.3$  and  $\sim 0.11$  for  $\mu_{p1}$  and  $\mu_{ss}$ ,  
271 respectively (Fig. 2b). Instead, the second  $\mu_{p2}$  disappeared with increasing normal  
272 stress (Fig. 2a).

273

274 **3.2 Microstructures, mineralogy and chemical composition of the solidified**



275 **frictional melt**

276 We recovered the experimental products of the slip-stepping experiments and  
277 investigated with OM, FESEM-EDX, synchrotron XRD and synchrotron TXM. The  
278 mineralogy and microstructures of the slipping zones are shown in Figures 4, 5, and 6.  
279 In general, the thickness of the experimental slipping zones increases from the edge  
280 (where the slip rate is the highest) to the center (where the slip rate is nominally zero) of  
281 the circular slip surface (Fig. 4a to d). In the experiment stopped at State A, the  
282 solidified melt patches were discontinuous and meniscus-shaped (Fig. 4). In the  
283 experiments stopped at states B and C, the solidified melt formed a continuous and  
284 dark-coloured donut-shaped feature. In the experiment stopped at State D, the  
285 solidified melt covered the entire slip surface (Fig. 4). In addition, the boundary  
286 solidified melt / host rock was irregular (presence of embayments, indicated by  
287 arrows in Figs. 4a-d) due to selective melting of the low-melting-point minerals (e.g.,  
288 muscovite) of the granitic gneiss (see Hirose and Shimamoto, 2003; Fig. 4d). The  
289 average thickness of the solidified frictional melt layers was determined by averaging  
290 the value of the real melt thickness obtained at different horizontal positions of the  
291 solidified melt on the slip surface. Although this measurement might result in an  
292 underestimate value as it includes the extrusion of melt at the end of slip, the melt  
293 thickness still notably varied at each state from ~ 270  $\mu\text{m}$  in State A, ~ 330  $\mu\text{m}$  in  
294 State B, ~ 170  $\mu\text{m}$  in State C, and ~ 230  $\mu\text{m}$  in State D (Table 2).

295 The *in-situ* synchrotron XRD data show that the mineral assemblage of the host  
296 rock (black line) was composed of quartz, feldspar, calcite, and muscovite (Fig. 4e).  
297 Instead, the clasts suspended in the solidified frictional melts produced in the  
298 slip-stepping experiments were mainly composed of quartz and minor feldspar  
299 (Fig. 4e). As observed in both natural and experimental pseudotachylytes, this  
300 indicates that quartz is more resistant than feldspar and muscovite during  
301 comminution and melting (see Spray, 2010, for a review). Unfortunately, the signals  
302 of the presence of amorphous materials (= glass matrix of the pseudotachylytes)  
303 between  $15^\circ$  to  $40^\circ$  of  $2\theta$  were not detected in the synchrotron XRD spectra because  
304 of the strong signal depression due to the high peaks of quartz.

305 Under the FESEM-BSE, the grains of the undeformed Hoping granitic gneiss are  
306 angular and elongated in shape, with grain size varying from ~0.1 to ~1.0 mm (not  
307 shown). The representative BSE images of the solidified melts under identical  
308 magnification show a substantial amount of sub-angular quartz grains and the  
309 presence of vesicles distributed within the glass matrix (Fig. 5). It is clear that the  
310 grain size distribution of the survivor grains of quartz varies significantly over the  
311 four states of the slip-stepping experiments, e.g., grains < 5  $\mu\text{m}$  in size in State C are  
312 more abundant than in both States B and D (Fig. 5 and section 3.5).

313 The TXM images show the overlapping of rounded to sub-rounded survivor  
314 grains which ranged from 50 nm to 10  $\mu\text{m}$  in diameter within the solidified melts  
315 representative of the four states of the slip-stepping experiments (Fig. 6). For grains <  
316 5  $\mu\text{m}$  (size range that is difficult to be clearly observed under SEM-BSE), we find that  
317 the shapes of the survivor grains in the TXM images were in rounded or spherical  
318 shape, similar occurrence to the survivor quartz grains reported from Kuo et al. (2015).  
319 These results suggest that partial melting on the edge of grains likely occurred, in  
320 particular, for ultra-fine grains (Kuo et al., 2015).

321 We utilized FESEM/EDS to analyze the matrix of the solidified frictional melts  
322 and adopted the average value of 40 points as representative of the chemical  
323 composition of the matrix (Table 1). The analysis showed no significant chemical  
324 variation of the composition of the solidified frictional melts from any of the four  
325 states of the slip-stepping experiments, except for the enrichment in  $\text{SiO}_2$ -content  
326 from State A to State C and particular high CaO-content in State D. The Raman  
327 spectra of the slip-stepping experiments showed negligible water content in the  
328 solidified frictional melts (Fig. 7).

329

### 330 **3.3 Frictional melt viscosity and temperature estimate**

331 In addition to the measured temperature of the frictional melt during the  
332 experiment LHVR1097, we also estimated the possible viscosity and temperature of  
333 the friction melt in the four states following the method suggested by Wallace et al.  
334 (2019). The non-Arrhenian Newtonian temperature-dependence viscosity of the  
335 silicate melt can be estimated by the GRD viscosity calculator (available online at  
336 <https://www.eoas.ubc.ca/~krussell/VISCOSITY/grdViscosity.html>) by inputting the  
337 melt composition (table 1; Giordano et al., 2008; Lavallée et al., 2012). This  
338 calculation is based on the Vogel-Fulcher-Tamman equation:

$$339 \quad \text{Log} \eta = A + \frac{B}{T(K)-C} \quad \text{Eq. 5}$$

340 where the  $\eta$  is viscosity (Pa s),  $A$ ,  $B$ , and  $C$ , are the modelled parameters based on  
341 viscosity measurement of geochemical composition (Giordano et al., 2008), and  $T$  the  
342 silicate melt temperature ( $K$ ). We obtained the viscosity curves for the slip-stepping  
343 frictional melts (Fig. 8) by giving at the constant  $A$  the value of -4.55 (optimal value  
344 based on Giordano et al. (2008)), and the values of  $B$  and  $C$  were obtained from the  
345 chemical composition of the glasses and 17 adjustable parameters (see demonstration  
346 calculation in Giordano et al. (2008), Table 1). The presence of vesicles suggests that  
347 some volatiles (e.g., OH from muscovite) were present in the melt, but the water  
348 content in the glass was likely negligible and assumed to be zero based on the absence  
349 of water signal from Raman analysis (Fig. 7).

350 Based on the mechanical data, the apparent viscosity of the frictional melts ( $\eta_{app}$ )  
351 can be directly calculated by the ratio of the measured shear stress to the strain rate as:

$$352 \quad \eta_{app} = \frac{\tau}{\dot{\epsilon}} = \frac{\tau w}{V_e} \text{ [Pa s]} \quad \text{Eq. 6}$$

353 where  $\tau$  is the measured shear stress (Pa),  $\dot{\epsilon}$  is the strain rate ( $s^{-1}$ ),  $w$  is the thickness  
354 of the melt layer (an underestimate of the thickness during sliding as it includes the  
355 extrusion of melt at the end of slip) and  $V_e$  is the equivalent slip velocity (m/s).  
356 Because solid particles (= survivor clasts) are present in the frictional melts, the  
357 calculated apparent viscosity could be overestimated (e.g., Metzner, 1985). To correct  
358 the effect of clasts on the apparent viscosity, we calculated the relative viscosity ( $\eta_r$ )  
359 using an empirical equation (Kitano et al., 1981):

$$360 \quad \eta_r = \left(1 - \frac{\phi}{A}\right)^{-2} \quad \text{Eq. 7}$$

361 with  $A = 0.54 - 0.0125r$ , where  $\phi$  is the volume fraction (volume particles/total volume)  
362 of the clasts,  $A$  is the parameter related to the packing geometry of the solid particles  
363 and  $r$  is the average aspect ratio of solid grains (about 2 in our case). We measured the  
364  $\phi$  using BSE images from the center to the edge of the experimental pseudotachylyte  
365 and averaged the value. The value of  $\phi$  ranged from  $\sim 0.11$  at State C to  $\sim 0.20$  at State  
366 A, B, and D (Table 2). Moreover, the presence of vesicles should lower the apparent  
367 viscosity of the frictional melt (e.g. Manga et al., 1998). However, the volume fraction  
368 of the vesicles is small ( $< 0.1$ ) and shows no significant variation in the four states.  
369 Therefore, the contribution of the vesicles to the apparent viscosity should be  
370 negligible (Lejeune et al., 1999). Based on Eqs. 6 and 7, the mechanically-constraint  
371 apparent viscosities corrected with the presence of clasts ( $\eta_c = \eta_{app} / \eta_r$ ) are  $\sim 229$  Pa s  
372 at State A,  $\sim 232$  Pa s at State B,  $\sim 125$  Pa s at State C, and  $\sim 99$  Pa s at State D (Table  
373 2).

374 According to the model for Non-Arrhenian temperature-dependence of melt  
375 viscosity (Eqs. 5; Wallace et al., 2019), the chemically- and mechanically-constraint  
376 apparent viscosities for the four states are consistent with the temperature of  $\sim 1370^\circ\text{C}$   
377 (State A),  $\sim 1300^\circ\text{C}$  (State B),  $\sim 1456^\circ\text{C}$  (State C), and  $\sim 1265^\circ\text{C}$  (State D) (Fig. 8).  
378 These chemo-mechanical-constraint temperature estimates are at odds with the  
379 temperature measured estimated with the infrared camera, as it will be discussed in  
380 section 4.3.

381

### 382 **3.4 Particle size distribution (PSD)**

383 The PSD was obtained by measuring all clasts (mainly made of quartz) within

384 the solidified frictional melt from the images of both SEM and TXM. With the  
385 FESEM, for each state, we collected eight to twelve BSE contiguous images to cover  
386 almost entirely slipping zone. Moreover, we collected some images at higher  
387 magnification (1,300X, similar to Fig. 5) to obtain more accurate size distribution on  
388 finer grains ( $< 10 \mu\text{m}$ ). With the TXM, for each state, we analyzed identical areas of  
389  $375 \mu\text{m}$  in length and  $75 \mu\text{m}$  in width, corresponding to the central part of the slipping  
390 zone. Since the TXM images included all the grains over the entire thickness ( $30 \mu\text{m}$ )  
391 of the thin-section, the number of particles measured from the TXM images has  
392 different unit compared to that from BSE images (i.e. number of particles per  $\mu\text{m}^2$  for  
393 SEM and per  $\mu\text{m}^3$  for TXM). Therefore, we further divided the obtained data from the  
394 TXM images by the sample thickness ( $\mu\text{m}$ ) to integrate it with the PSD data from the  
395 BSE images. To increase the accuracy of the density data in size range of  $1\text{--}3 \mu\text{m}$   
396 (lower limit of SEM analysis), we extend the TXM results to overlap this size range.  
397 The density data in this overlapping range is reported as the average value of both  
398 TXM and SEM results.

399 The PSD data were plotted as a cumulative frequency diagram for the mean  
400 diameter,  $r$ , using a logarithmic scale. Our results (solid dots) were fitted and plotted  
401 with solid curves for mean diameters  $> 1 \mu\text{m}$  and as dashed lines for diameters  $< 1 \mu\text{m}$ .  
402 The particle density,  $N(r)$ , which represents the cumulative number of particles per  
403  $\mu\text{m}^2$ , follows a function of mean diameter ( $r$ ), defined as the geometric mean of the  
404 major and minor axes of an irregular grain, in the form of a power-law for frictional  
405 melting (not comminution):  $N(r) = N'(1 + r/r')^{-D}$ , where  $N$  is the cumulative number  
406 of grain sizes greater than  $r$ , that is,  $N'$  (which depends on the total number of  
407 measurements),  $r'$  is constant, and  $D$  is the fractal dimension (Shimamoto and  
408 Nagahama, 1992; Tsutsumi, 1999).

409 The fitted curves for each state are almost identical, i.e., the curves are steep in  
410 the coarse-grained size ranges ( $> 10 \mu\text{m}$ ) and gently flatten towards fine size  $< 10 \mu\text{m}$ ,  
411 and to some degree the PSDs obey to a power-law (Fig. 9). Interestingly, we find that  
412 the measured particle density for the grain sizes smaller than  $1 \mu\text{m}$  is larger than the  
413 fitted curves, in particular, at states A and B (Fig. 9). Based on the previous PSD  
414 studies of the experimentally produced pseudotachylytes, the slope of the PSD curves  
415 shows a linearly steep to horizontal evolution in the size range from about  $100 \mu\text{m}$  to  
416  $0.5 \mu\text{m}$  (e.g. Tsutsumi, 1999, Fig. 2). These curves were obtained from the solidified  
417 melt with long displacement experiments (hundreds of meters) and the change of the  
418 slope was suggested to be the effect of partial melting of the survivor grains.  
419 Therefore, compared to our results obtained from the short-displacement experimental  
420 melt ( $< 3 \text{ m}$ ), the deviation between measured density data and fitted curves in size  $<$

421 1  $\mu\text{m}$ , particularly significant in States A and B, may suggest that the ultra-fine quartz  
422 grains derived from the surface comminution are trapped in the melts. Instead, the  
423 PSD of the clasts from State C is described by a larger value for  $D$ . The reduced  
424 thickness of the slipping zone during frictional melting is one of the factors  
425 controlling the size reduction of the clasts in the coarse-grained range and, as a  
426 consequence, the fractal dimension of their distribution (Tsutsumi, 1999). In addition,  
427 thickness of the melt zone might strongly depend on the viscosity and thus on the  
428 temperature of the melt layer. This may suggest the high value of  $D$  at State C might  
429 be controlled by the melt thickness (the thinnest among the slip-stepping experiments).  
430 But here we cannot evaluate how the size reduction and melt viscosity influence the  $D$   
431 value due to their complicated correlation and more comprehensive studies are  
432 required.

433

#### 434 **4. Discussion**

##### 435 **4.1 Frictional evolution during fast fault slip at low normal stress**

436 We focus on the complicated frictional evolution of granitic melts at low normal  
437 stress. Chen et al. (2017b) performed frictional experiments on granitic rocks for  
438 moderate velocities (0.01–0.11 m/s) to investigate the complicated frictional evolution  
439 with slip at the transition between powder lubrication and melt lubrication. They  
440 suggested that the evolution of the frictional behavior can be divided into three stages  
441 based on different physical mechanisms: the initial weakening stage (Stage 1: powder  
442 lubrication), the initial strengthening stage (Stage 2: viscous melt patches), and the  
443 final weakening stage (Stage 3: melt lubrication) (Fig. 10a). They concluded that this  
444 complicated frictional evolution is the result of thermally-activated deformation  
445 processes. In the discussion below, we exploit the conceptual model proposed by  
446 Chen et al. (2017b) to our experimental dataset. At slip initiation, during Stage 1, we  
447 propose that flash heating and melting of the asperity contacts is the dominant  
448 weakening mechanism once a threshold sliding velocity of  $> 0.1$  m/s (case for  
449 silicate-built rocks) is achieved (Rice, 2006; Di Toro et al., 2006b; Hirose and  
450 Shimamoto, 2005; Niemeijer et al., 2011; Goldsby and Tullis, 2011; Proctor et al.,  
451 2014; Violay et al., 2014a; Fig. 10b-e). Then, we divide the Stage 2 of Chen et al.  
452 (2017b) (dynamic fault strengthening in the presence of powders and melt patches)  
453 into States A (first peak), B, and C (second peak) and keep Stage 3 of Chen et al.  
454 2017b (weakening due to the presence of a continuous melt layer) as our State D (see  
455 also discussion in Hirose and Shimamoto, 2005; Di Toro et al., 2006b; Niemeijer et al.,  
456 2011; Violay et al., 2014b; Proctor et al., 2014) (Fig. 10b-e). Below we focus on the  
457 complex frictional evolution during Stage 2.

458

459 **4.2 Initial strengthening in Stage 2 (State A)**

460 At slip initiation, when flash heating occurs, temperatures significantly rise at the  
461 asperity scale and melt the rock contacts (Rice, 2006). In addition, rubbing of the  
462 asperity contacts induces tribo-chemical reactions and triggers different mechanisms.  
463 Therefore, tribo-chemical reactions may occur at lower activation energies (and thus  
464 their kinetics is more efficient at a given temperature) than thermo-chemical reactions  
465 (Steinike and Tkáčová, 2000). It is reasonable to assume that flash heating of the  
466 granitic gneiss may result in the preferential fusion of the low melting point minerals  
467 (i.e., muscovite,  $T_m = 650^{\circ}\text{C}–900^{\circ}\text{C}$  at 1 atm; Spray, 2010, see discussion below) but  
468 also in the formation of silica-rich melt droplets from fusion of high melting point  
469 minerals as quartz (main mineral of the gneiss,  $T_m = 1720^{\circ}\text{C}$  at 1 atm; Spray, 2010).  
470 The melt patches in State A were derived from the accumulation of the melt droplets  
471 produced by flash heating and melting at the asperity contacts, resulting in the  
472 formation of relatively silica-rich melts.

473 In addition, the PSD data of State A shows the presence of ultra-fine grains,  
474 suggesting an additional source of grains into the melt. When frictional melts  
475 occurred and covered the entire slip surface, the survivor grains were mainly derived  
476 from thermal cracking and frictional melting of the wall rocks and sticking out from  
477 the wall rocks into the melt. Based on this, compared to the PSD of State D, we  
478 conclude that the additive grains in State A were the result of mixtures of rock clasts  
479 (by rock fragmentation) and melt patches during initial sliding.

480 The temperature measured with the infrared camera at State A is  $\sim 500^{\circ}\text{C}$ , and it  
481 is likely an underestimated because of (1) averaging with the slipping zone and the  
482 wall-rocks and (2) slightly unfocused measuring (outside of the slipping zone).  
483 Integrated with the mineralogical observation (Fig. 4e), the temperature at State A  
484 should achieve the breakdown point of muscovite (at least  $> 650^{\circ}\text{C}$ ) and was  
485 relatively lower than the other states (with shorter slip and less frictional work input;  
486 see the details in section 4.3). Therefore, the estimated temperature and corresponding  
487 viscosity (Fig. 8 and Table 1) indicate that the silica-rich melt patches of State A were  
488 highly viscous and presumably contributed to the resistance of shearing, resulting in  
489 the initial strengthening in Stage 2, similar to the observation reported by Chen et al.  
490 (2017b).

491

492 **4.3 Re-strengthening in Stage 2 (states B to C)**

493 With progressive sliding, the melt patches accumulated into a donut-shaped melt  
494 layer and the two rock specimen were partly separated from the melt layer (States A to  
495 B; Fig. 4b). Here, we simply neglect the contribution from solid-solid friction in the  
496 central part of the slip surface because the torque and thus the shear stress increase

497 with sample radius (e.g., Eq. 2), where the frictional contribution from the inner part  
498 of the cylinder is negligible (Hirose and Shimamoto et al., 2005). In addition, because  
499 the microstructural observation shows that solidified melts were thicker than the  
500 surface roughness (Fig. 4), the solid-solid contacts at the outer melt regime were  
501 unlikely to have occurred. We suggest that donut-shape melt layer is the main  
502 contribution for shear resistance during the experiment. As a consequence, melt  
503 viscosity and shear strain rate are the dominant parameters that control the shear  
504 resistance of the simulated fault during the frictional melting regime (States B to D).

505 Melt viscosity is controlled by three parameters: temperature, presence of water,  
506 and chemical composition (Lejeune et al., 1999; Fluegel et al., 2004). According to  
507 the mechanically-constraint viscosity model (section 3.3), the temperatures achieved  
508 in States A to D are about 1370°C, 1300°C, 1456°C, and 1265°C, respectively (Fig. 8).  
509 The estimated temperature of State D (melt lubrication regime) is in good agreement  
510 with previous rock friction experiments conducted at seismic slip rates (Hirose &  
511 Shimamoto, 2005; Di Toro et al., 2006; Niemeijer et al., 2011, 2012; Nielsen et al.,  
512 2008). The estimated temperature of State D (1265°C) can be set as the upper bound  
513 for the temperature achieved in the slip-stepping experiments. In fact, the temperature  
514 achieved in States A to C should be lower than the one achieved during State D  
515 because, under the same conditions, the shorter slip also imply less work input by the  
516 motor. Therefore, according to the evaluation of temperature at State D, the estimated  
517 temperature of State C (1456°C) is overestimated.

518 On the basis of the mineralogy of the survivor clasts (e.g., muscovite was melted  
519 through all the slip-stepping experiments; Fig. 4e), we can take the melting point of  
520 muscovite into consideration to estimate the temperature of the friction melt. The  
521 melting point ( $T_m$ ) of muscovite during static heating at a low heating rate of 1°C/min  
522 is 650°C (Spray, 2010) and  $T_m$  increases to 900 °C at a high heating rate of 200 °C/min  
523 (Kuo et al., 2011). Because of the difficulty of evaluating on one side the contribution  
524 of grinding processes during frictional sliding that may further lower the  $T_m$  of  
525 muscovite and, on the other side the heating rate which is much higher than the  
526 aforementioned heating rates tested in the laboratory (e.g., Kuo et al., 2011), we  
527 assume that the lower bound of the temperature achieved during States B and C is  
528 ~900°C.

529 In experiment LHVR1097 we measured the temperature evolution from States A  
530 to D (Fig. 3e). The temperature measured by the infrared camera is affected by (1)  
531 absorption (i) of emitted radiance by gases produced during frictional sliding (SO<sub>2</sub>,  
532 H<sub>2</sub>O, CO<sub>2</sub>) and (ii) of the powders suspended in the air, (2) variance of emissivity ( $\epsilon$ ),  
533 and (3) the thickness of the slipping zone which is thinner than the area investigated  
534 by the infrared camera (i.e., the camera measures the temperature over an area that

535 includes both the hot slipping zone and the cold wall rocks). As a consequence, the  
536 temperature measured with the infrared camera is commonly considered as an  
537 underestimated value. Abtahi et al. (2002) reported that broadband emissivity  
538 systematically rises as the lava cools, from 0.55 at 1050°C to 0.85 at <500°C. In our  
539 case, the widespread preferential melting of muscovite demonstrates that temperatures  
540 were higher than 650°C in the slipping zones of States A to D. As a consequence, it  
541 seems that a low value of emissivity ( $\varepsilon = 0.55$ ) is more appropriate for the temperature  
542 measurements with the infrared camera, and thus, the associated estimated  
543 temperature is ~850°C, as the lower bound of temperature of States B and C. Taken  
544 together, the achieved temperatures for States A to C should be in the range of 850°C  
545 to 1265°C (the pink area in Fig. 8).

546 In the temperature range of 850°C to 1265°C, the viscosity of the melt in State C  
547 is higher than the one achieved in the other states ( $10^{8.0}$ – $10^{3.1}$  Pa s,  $10^{7.7}$ – $10^{2.7}$  Pa s,  
548  $10^{8.2}$ – $10^{3.3}$  Pa s for States A to C, respectively). In addition, the slope of the  
549 Non-Arrhenian temperature dependence of the viscosity curves become less steep.  
550 This suggests that even if the temperature of the melt increases with slip between  
551 States B and C (i.e. temperature at State C is slightly higher than the one at State B;  
552 Fig. 3e), the estimated viscosity at State C can be higher than the one at State B.

553 To summarize, because of frictional heating, the bulk temperature in the slipping  
554 zone increases with slip (Fig. 3e) and likely reduces the melt viscosity, resulting in  
555 melt lubrication (Di Toro et al., 2006). However, by itself, the gradual temperature  
556 increase, which would result in less viscous friction melts, is at odds with the  
557 re-strengthening behavior (i.e.,  $\mu_{p2}$  occurred at an higher temperature than  $\mu_{p1}$ ; Figs. 2  
558 and 3e). On the basis of the temperature-viscosity model (Fig. 8), the evolution of the  
559 chemical composition of the frictional melt with slip might be the most plausible  
560 explanation for re-strengthening from State B to C. Though water was present at the  
561 initiation of slip (the experiments were performed under room-humidity conditions)  
562 and released by the breakdown of muscovite, because of the not-confined conditions,  
563 gases could escape from the frictional melt. This resulted in the formation of vesicles  
564 and in the negligible water content of the pseudotachylyte matrix (Raman  
565 spectroscopy data in Fig. 7). As a consequence, water cannot be responsible for the  
566 variation of the viscosity of the melt in any of the States. On the other hand, the  
567 experiment s1286 under vacuum conditions (Table 1) may further indicate the  
568 re-strengthening is irrelevant to the humidity and/or oxidation. Taken together, the  
569 increase in SiO<sub>2</sub> in the frictional melt might be the most plausible contributor for the  
570 re-strengthening from State B to State C (Table 1).

571 The presence of clasts made of quartz and, to a less extent, feldspar and the  
572 absence of muscovite in the solidified frictional melt (Figs. 4e, 5) suggest that



573 selective melting of low-melting-point minerals (i.e., muscovite) took place (Shand,  
574 1916; Sibson, 1975; Spray, 1987). However, the chemical composition of the glass  
575 matrix at States B and C is higher in SiO<sub>2</sub> and lower in CaO (Table 1) compared to the  
576 composition of the glass matrix at State D which was produced at higher temperatures  
577 (Fig. 3e). This chemical variation suggests that partial melting of quartz was more  
578 efficient at States B and C than State D while partial melting of feldspar was  
579 comparatively efficient at State D. In fact, during State D the sliding surfaces were  
580 entirely separated by the frictional melt (Fig. 4d) and grain fragmentation due to  
581 solid-solid contact of the asperities was less efficient than during States A to C.  
582 Therefore, the presence of rock powders (mostly made by quartz and feldspar) in the  
583 frictional melts likely drove further melting of the small grains by quasi-equilibrium  
584 melting (Lee et al., 2017) or by the Gibbs-Thomson effect due to the high  
585 surface-to-area ratio (Hirose and Shimamoto, 2003). These particular melting  
586 processes resulted in the increase of Ca (although not obvious in our result) and  
587 especially Si content in the frictional melt and, as a consequence, in the increase of  
588 the melt viscosity from State B to State C (Table 1). Without the addition of  
589 fragmentation products, the chemical composition of the glass matrix at State D was  
590 then mainly derived from the melting of feldspar and muscovite.

591 We propose that the enrichment in Si in the frictional melt associated to  
592 grain-by-grain fragmentation at the initiation of simulated seismic slip may explain  
593 the observed fault re-strengthening observed in previous experiments performed at  
594 seismic rates (Di Toro et al., 2006b; Hirose and Shimamoto, 2005; Niemeijer et al.,  
595 2011) (Fig. 10). Moreover, this process of chemical evolution of melt composition  
596 with slip also support the model proposed by Fialko and Khazan (2005) according to  
597 which thermal-activated slip strengthening is likely to occur in quartz-rich rocks at  
598 shallow depths.

599

#### 600 **4.4 Final weakening during Stage 3 (State C to D)**

601 The final fault weakening is observed in all the experiments, but of course not in  
602 the short slip-stepping experiments (Fig. 2b), and is associated to the formation of a  
603 continuous frictional melt layer (Fig. 4d). In fact, frictional melts with high  
604 temperatures and low silica content (Table 1) are an efficient lubricant, consistently  
605 with previous experimental and theoretical studies (Hirose & Shimamoto, 2005; Di  
606 Toro et al., 2006a, b; Niemeijer et al., 2011, 2012; Nielsen et al., 2008). In addition,  
607 our mechanical data are comparable to those of previous experiments on tonalite  
608 (similar mineral assemblages without foliation) where both data show low effective  
609 friction coefficient (0.13 and 0.05, respectively) at the steady-state melting (Di Toro et  
610 al., 2006a, b). This suggests that the mineralogical heterogeneity of the specimens due

611 to the metamorphic foliation makes only a very minor influence on the obtained  
612 values of shear stress.

613

#### 614 **4.5 Rock friction experiments and Re-strengthening behavior**

615 The mechanical data shows a complicated evolution of the friction coefficient  
616 (flash weakening, first strengthening, slight weakening, second strengthening, and  
617 eventually weakening) with slip at low normal stresses ( $< 10$  MPa) (Fig. 2a). This  
618 complicated evolution almost disappears and approximates an exponential decay at  
619 larger normal stresses (e.g., 30 MPa) (Fig. 2a). The most significant change with  
620 increasing normal stress is the reduction of the first peak value  $\mu_{p1}$  and the  
621 disappearance of the second peak  $\mu_{p2}$  (Fig. 2a). This is the result of the more  
622 continuous transition from flash weakening to melt lubrication with increasing normal  
623 stress, but also with increasing slip rate and slip acceleration rate (5 m/s and 6.5 m/s<sup>2</sup>,  
624 respectively, for the experiments performed with SHIVA). In fact, the higher heat  
625 production rate, proportional to the product of the normal stress per slip rate,  
626 dissipated on the slipping zone results in the fast generation of the frictional melt and  
627 rapid reduction of the friction coefficient. Therefore, at larger normal stresses and slip  
628 rates, the effect of surface comminution becomes negligible during the onset of slip.

629 In the case of the experiments performed with SHIVA, sample preparation  
630 (pre-grounding process) can influence the frictional evolution with slip. Niemeijer et  
631 al. (2011) pre-grounded the samples with SHIVA to achieve perfect alignment and  
632 obtained a complicated friction evolution afterward. It seems that, by doing this,  
633 ultra-fine powders were likely generated and potentially stuck on the asperities of the  
634 slip surface, even though the powder was cleaned with an air brush before the  
635 high-speed experiment. Nielsen et al. (2012) applied a new method to align the  
636 SHIVA samples without pre-grinding the slip surfaces and obtained a simpler  
637 evolution (which approximated an exponential decay) of the friction coefficient at slip  
638 initiation (Violay et al., 2014a,b; Violay et al., 2019). Therefore, both SHIVA and  
639 LHVR results demonstrate the presence of a correlation between the presence of  
640 fragments in the slipping zone and the second re-strengthening behavior.

641

#### 642 **4.6 Implications for natural Hoping pseudotachylyte**

643 We apply our experimental results to the natural observations of the Hoping  
644 pseudotachylyte. Ferré et al. (2016) proposed to use a novel linear structure  
645 decorating the slip surfaces of pseudotachylytes, described as "brushlines", to identify  
646 the coseismic slip direction. The brushlines were suggested to form through viscous  
647 brushing between protruding asperities of the host rocks and the viscous frictional  
648 melt (solid-liquid interaction) during rapid cooling at the end of slip. The chemical

649 compositions of the Hoping pseudotachylyte (average 61% silica content, Kuo, 2016)  
650 and of the experimental pseudotachylytes from the same rocks generated in State C  
651 (Table 1) are very similar. It implies that the Hoping pseudotachylyte likely formed  
652 during small seismic slip events or at the initial fault sliding (corresponding to State B  
653 to C) and contained remnant grains from fault comminution. If so, our finding about  
654 the chemically induced increased viscosity of the frictional melt might be another  
655 explanation for the process of viscous brushing.

656

## 657 **5. Conclusions**

658 In this study, we present the mechanical results of slip-stepping experiments  
659 performed on solid cylinders of granitic gneisses sheared at high slip velocities using  
660 rotary shear machines (SHIVA and LHVR) coupled with high-resolution  
661 microstructural (scanning electron microscope, Transmission X-ray microscopy,  
662 image analysis, etc.) and mineralogical (synchrotron X-ray diffraction analysis,  
663 micro-Raman spectroscopy, etc.) investigations of the experimental fault products. In  
664 the case of the experiments performed at seismic slip rates (1.3 to 5 m/s) but low normal  
665 stress ( $< 10$  MPa), the mechanical data show a complicated frictional evolution with  
666 slip which includes: initial weakening, first strengthening followed by a slight  
667 decrease and then by a second strengthening and a final exponential decay towards a  
668 steady state value (Figs. 2-3). This complex frictional evolution becomes less  
669 pronounced in the experiments performed at larger normal stresses and is associated  
670 with the evolution of the viscosity of the frictional melts (chemical composition,  
671 temperature, etc.) (Figs. 4-9 and Table 1). We thus modified the model of Chen et al.  
672 (2017b) for the various friction behaviors (stages 1 to 3) associated with different  
673 physical mechanisms (Fig. 10). We propose that the initial fault weakening is due to the  
674 grain fragmentation and flash heating and weakening on bare rock surfaces. The first  
675 fault strengthening is due to braking from the formation of a highly viscous (also  
676 because of the low temperature) frictional melt. The second fault re-strengthening is  
677 associated with the increased viscosity mainly because of the  $\text{SiO}_2$  enrichment of the  
678 frictional melt. The increase in  $\text{SiO}_2$  content is probably due by a combination of  
679 quasi-equilibrium melting and the Gibbs-Thomson effect on the ultra-fine quartz  
680 grains. The final weakening is due to melt lubrication because of the formation of a  
681 continuous melt layer covering the entire slip surface together with the reduction of the  
682 viscosity because of the increased temperature of the melt.

683 Considering the experimental conditions at which the chemically-induced high  
684 viscosity frictional melt forms, we suggest that the surging of frictional melts  
685 generated behind the rupture front likely hampers seismic slip during initial  
686 earthquake propagation at shallow depths, even though melt lubrication takes place

687 afterward. As a natural example, although the Hoping pseudotachylytes were  
688 generated at depths > 4km, our result suggests that the chemically-induced high  
689 viscosity frictional melt formed in the Hoping area may therefore play a braking role  
690 during fault rupture into shallow depths.

691

### 692 **Acknowledgements**

693 This research was supported by the European Research Council Consolidator  
694 Starting Grant 614705 NOFEAR to Giulio Di Toro and Taiwan ROC (Republic of  
695 China) Ministry of Science and Technology (MOST 108-2116-M-008-021-MY2) to  
696 Li-Wei Kuo. Samples were prepared by Jialiang Si via the National Science  
697 Foundation of China (41572192, 41330211). We thank Taiwan Power Company and  
698 Industrial Technology Research Institute for providing the Hoping borehole cores, and  
699 Dr. Che-Ming Yang and Hsiu-Ching Hsiao for their laboratory support. The  
700 experimental data supporting this work are publicly available online  
701 (<http://140.115.20.219:5000/sharing/VTj4nVZcU>).

702

### 703 **References cited**

- 704 Abtahi, A.A., Kahle, A.B., Abbot, E.A., Gillespie, A.R., Sabol, D., Yamada, G., and  
705 Pieri, D.C. (2002), Emissivity changes in basalt cooling after eruption from Pu'u  
706 O'o [abs.]: Eos (Transactions, American Geophysical Union), 83, no.  
707 V71A-1263.
- 708 Beeler, N., T. Tullis, and D. Goldsby (2008), Constitutive relationships and physical  
709 basis of fault strength due to flash heating, *J. Geophys. Res.*, 113, B01401,  
710 doi:10.1029/2007JB004988.
- 711 Brodsky, E. E. and Kanamori, H. (2001), Elastohydrodynamic lubrication of faults. *J.*  
712 *Geophys. Res.* 106, 16,357–16,374, doi: 10.1029/2001JB000430.
- 713 Bürgmann, R., and G. Dresen (2008), Rheology of the lower crust and upper mantle:  
714 Evidence from rock mechanics, geodesy, and field observations, *Annual Review*  
715 *of Earth and Planetary Sciences*, v. 36, p. 531–567, doi: 10 .1146  
716 /annurev .earth .36 .031207 .124326.
- 717 Byerlee, J. (1978), Friction of rocks, *Pure Appl. Geophys.*, 116, 615–626, doi:  
718 10.1007/BF00876528.
- 719 Carslaw, H., and J. Jaeger (1959), *Conduction of Heat in Solids*, vol. 19591,  
720 Clarendon Press, Oxford, doi: 10.1007/978-1-4939-2565-0\_2.
- 721 Chen, X., A. S. E. Madden, and Z. Reches (2017a), Powder-rolling as a mechanism of  
722 dynamic fault weakening, In M. Thomas, T. Mitchell, & H. Bhat (Eds.), *Fault*  
723 *zone dynamic processes: Evolution of fault properties during seismic rupture* (pp.  
724 133–150). Washington, DC and Hoboken, NJ: American Geophysical Union and

725 John Wiley, doi: 10.1002/9781119156895.ch7.

726 Chen, X., A. S. E. Madden, and Z. Reches (2017b), Friction evolution of granitic  
727 faults: heating controlled transition from powder lubrication to frictional melt, *J.*  
728 *Geophys. Res.*, doi: 10.1002/2017JB014462.

729 Chen, C.-T., C.-Y. Wu, C.-H. Lo, H.-T. Chu, and T.-F. Yui (2017), Dating palaeo-  
730 seismic faulting in the Taiwan Mountain Belt, *Terra Nova*, v. 30, issue 2, doi:  
731 10.1111/ter.12319.

732 Chu, H.-T., S.-L. Hwang, P. Shen, and T.-F. Yui (2012), Pseudotachylyte in the  
733 Tananao Metamorphic Complex, Taiwan: Occurrence and dynamic phase  
734 changes of fossil earthquakes, *Tectonophysics*, v. 581, p. 62–75, doi:  
735 10.1016/j.tecto.2012.01.017.

736 Collettini, C., C. Viti, T. Tesei, and S. Mollo (2013), Thermal decomposition along  
737 natural faults during earthquakes, *Geology*, 41, 923–930. doi:10.1130/G34421.1.

738 Cornelio, C., E. Spagnuolo, G. Di Toro, S. Nielsen and M. Violay (2019), Mechanical  
739 behavior of fluid-lubricated faults, *Nature Communications*, 10:1274, doi:  
740 10.1038/s41467-019-09293-9.

741 De Paola, N., Holdsworth, R.E., Viti, C., Collettini, C., Bullock, R., (2015), Can grain  
742 size sensitive flow lubricate faults during the initial stages of earthquake  
743 propagation? *Earth Planet. Sci. Lett.* 431, 48–58, doi: org /10 .1016  
744 /j.epsl .2015 .09 .002.

745 Di Toro, G., D. L. Goldsby, and T. E. Tullis (2004), Friction falls towards zero in  
746 quartz rock as slip velocity approaches seismic rates, *Nature*, 427, 436–439, doi:  
747 10.1038/nature02249.

748 Di Toro, G., G. Pennacchioni, and G. Teza (2005), Can pseudotachylytes be used to  
749 infer earthquake source parameters? An example of limitations in the study of  
750 exhumed faults, *Tectonophysics*, 402, 3–20, doi: 10.1016/j.tecto.2004.10.014.

751 Di Toro, G., T. Hirose, S. Nielsen, G. Pennacchioni, and T. Shimamoto (2006a),  
752 Natural and experimental evidence of melt lubrication of faults during  
753 earthquakes, *Science*, 331, 647–649, doi: 10.1126/science.1121012.

754 Di Toro, G., T. Hirose, S. Nielsen, and T. Shimamoto (2006b), Relating high-velocity  
755 rock-friction experiments to coseismic slip in the presence of melts, in *Radiated*  
756 *Energy and the Physics of Earthquake Faulting*, *Geophys. Monogr. Ser.*, vol. 170,  
757 edited by R. Abercrombie et al., pp. 121–134, AGU, Washington, D. C., doi:  
758 10.1029/170GM13.

759 Di Toro, G., A. Niemeijer, A. Tripoli, S. Nielsen, F. Di Felice, P. Scarlato, G. Spada, R.  
760 Alessandrini, G. Romeo, G. Di Stefano, S. Smith, E. Spagnuolo, and S. Mariano  
761 (2010), From field geology to earthquake simulation: a new state-of-the-art tool  
762 to investigate rock friction during the seismic cycle (SHIVA), *Rendiconti Lincei*,

763 1–20, doi: 10.1007/s12210-010-0097-x.

764 Ferré, E. C., E.-C. Yeh, Y.-M. Chou, R.-L. Kuo, H.-T. Chu, and C. S. Korren (2016),  
765 Brushlines in fault pseudotachylytes: a new criterion for coseismic slip direction,  
766 *Geology* 44 (5), 395–398, doi:10.1130/G37751.1.

767 Fialko, Y., and Y. Khazan (2005), Fusion by earthquake fault friction: Stick or slip?, *J.*  
768 *Geophys. Res.*, 110, B12407, doi:10.1029/2005JB003869.

769 Giordano, D., J. K. Russell, and D. B. Dingwell (2008), Viscosity of magmatic liquids:  
770 a model, *Earth and Planetary Science Letters* 271, 123–134, doi:  
771 10.1016/j.epsl.2008.03.038.

772 Goldsby, D. L., and T. E. Tullis (2011), Flash heating leads to low frictional strength  
773 of crustal rocks at earthquake slip rates, *Science*, 334, 216–218, doi:  
774 10.1126/science.1207902.

775 Green, H. W., F. Shi, K. Bozhilov, G. Xia, and Z. Reches, (2015), Phase  
776 transformation and nanometric flow cause extreme weakening during fault slip,  
777 *Nat. Geosci.*, 8, 448–489, doi: 10.1038/ngeo2436

778 Han, R., T. Shimamoto, T., Hirose, J.-H. Ree and J. Ando (2007), Ultralow friction of  
779 carbonate faults caused by thermal decomposition, *Science* 316 (5826), 878–881,  
780 doi: 10.1126/science.1139763.

781 Han, R., T. Hirose, , and T. Shimamoto (2010). Strong velocity weakening and  
782 powder lubrication of simulated carbonate faults at seismic slip rates. *J. Geophys.*  
783 *Res.*, 115, B03412, doi: 10.1029/2008JB006136.

784 Hayashi, N. and A. Tsutsumi (2010), Deformation textures and mechanical behavior  
785 of a hydrated amorphous silica formed along an experimentally produced fault in  
786 chert, *Geophys. Res. Lett.* 37, L12305, doi: 10.1029/2010GL042943.

787 Hirose, T., and T. Shimamoto (2003), Fractal dimension of molten surfaces as a  
788 possible parameter to infer the slip-weakening distance of faults from natural  
789 pseudotachylites, *J. Struct. Geol.*, 25, 1569–1574, doi:  
790 10.1016/S0191-8141(03)00009-9.

791 Hirose, T., and T. Shimamoto (2005), Growth of molten zone as a mechanism of slip  
792 weakening of simulated faults in gabbro during frictional melting, *J. Geophys.*  
793 *Res.*, 110, B05202, doi: 10.1029/2004JB003207.

794 Kitano, T., T. Kataoka, and T. Shirota (1981), An empirical equation of the relative  
795 viscosity of polymer melts filled with various inorganic fillers, *Rheol. Acta*, 20,  
796 207–209, doi: 10.1007/BF01513064.

797 Korren, C. S., E. C. Ferré, E.-C. Yeh, Y.-M. Chou and H.-T. Chu (2016), Seismic  
798 rupture parameters deduced from a Pliocene fault pseudotachylyte in Taiwan, In  
799 M. Y. Thomas, T. M. Mitchell, and H. S. Bhat (Eds.), *Fault Zone Dynamic*  
800 *Processes: Evolution of Fault Zone Properties and Dynamic Processes During*

801 Seismic Rupture AGU Monograph, (p. 227). Washington, USA: American  
802 Geophysical Union, doi: 10.1002/9781119156895.ch2.

803 Kuo, L.-W., S.-R. Song, L. Huang, E.-C. Yeh and H.-F. Chen (2011), Temperature  
804 estimates of coseismic heating in clay-rich fault gouges, the Chelungpu fault  
805 zones, Taiwan, *Tectonophysics*, 502, 315–327, doi: 10.1016/j.tecto.2011.02.001.

806 Kuo, L.-W., H. Li, S. Smith, G. Di Toro, J. Suppe, S. R. Song, S. Nielsen, H. S. Sheu  
807 and J. Si (2014a), Gouge graphitization and dynamic fault weakening during the  
808 2008 Mw 7.9 Wenchuan earthquake, *Geology* 42, 47–50, doi: 10.1130/G34862.1.

809 Kuo, L.-W., H. C. Hsiao, S.-R. Song, H. S. Sheu and J. Suppe (2014b), Coseismic  
810 thickness of principal slip zone from the Taiwan Chelungpu fault Drilling  
811 Project-A (TCDP-A) and correlated fracture energy, *Tectonophysics*, 619–620,  
812 29–35, doi: 10.1016/j.tecto.2013.07.006.

813 Kuo, L.-W., Y.-F. Song, C.-M. Yang, S.-R. Song, C.-C. Wang, J.-J. Dong, J. Suppe,  
814 and T. Shimamoto (2015), Ultrafine spherical quartz formation during seismic  
815 fault slip: Natural and experimental evidence and its implications, *Tectonophysics*,  
816 664, 98–108, doi: 10.1016/j.tecto.2015.09.008.

817 Kuo, R.-L. (2016). Microstructural and Magnetic Investigations of Pseudotachylyte  
818 and Ultracataclasite in the Hoping River, Tananao Complex, Eastern Taiwan.  
819 Unpubl. M.Sc. thesis, National Taiwan University, Taipei, Taiwan, R.O.C.

820 Lavallée, Y., T. M. Mitchell, M. J. Heap, J. Vasseur, K.-U. Hess, T. Hirose and D. B.  
821 Dingwell (2012), Experimental generation of volcanic pseudotachylyte:  
822 constraining rheology, *J. Struct. Geol.* 38, 222–233, doi:  
823 10.1016/j.jsg.2012.02.001.

824 Lee, S. K., R. Han, E. J. Kim, G. Y. Jeong, H. Khim and T. Hirose (2017),  
825 Quasi-equilibrium melting of quartzite upon extreme friction, *Nature Geoscience*,  
826 10, 436–441, doi: 10.1038/ngeo2951.

827 Lejeune, A. M., Bottinga, Y., Trull, T. W., Richet, P. (1999), Rheology of  
828 bubble-bearing magmas, *Earth Planet. Sci. Lett.* 166, 71–84, doi:  
829 10.1016/S0012-821X(98)00278-7.

830 Lin, A. and T. Shimamoto (1998), Selective melting processes as inferred from  
831 experimentally generated pseudotachylytes, *J. Asian Earth Sci.*, 16, 533–545, doi:  
832 10.1016/S0743-9547(98)00040-3.

833 Lin, A (2008), Fossil earthquakes: The formation and preservation of  
834 pseudotachylytes, Berlin Heidelberg: Springer-Verlag, doi:  
835 10.1007/978-3-540-74236-4.

836 Manga, M., J. Castro, K. V. Cashman, and M. Loewenberg (1998), Rheology of  
837 bubble-bearing magmas, *J. Volcanol. Geotherm. Res.*, 87, 15– 28, doi:  
838 10.1016/S0377-0273(98)00091-2.

839 Metzner, A. B. (1985), Rheology of suspensions in polymeric liquids, *J. Rheol.*, 29,  
840 739–775, doi: 10.1122/1.549808.

841 Nielsen, S., G. Di Toro, T. Hirose, and T. Shimamoto (2008), Frictional melt and  
842 seismic slip, *J. Geophys. Res.*, v. 113, no. B01308, doi: 10.1029/2007JB005122.

843 Nielsen, S., E. Spagnuolo, and M. Violay (2012), The ultimate sample preparation for  
844 rotary shear experiments. *Rapporti tecnici INGV*,  
845 (<http://istituto.ingv.it/1-ingv/produzione-scientifica/rapporti-tecnici-ingv/numeri-pubblicati-2012>).  
846

847 Niemeijer, A., G. Di Toro, S. Nielsen, and F. Di Felice (2011), Frictional melting of  
848 gabbro under extreme experimental conditions of normal stress, acceleration, and  
849 sliding velocity, *J. Geophys. Res.*, 116, B07404, doi: 10.1029/2010JB008181.

850 Niemeijer, A., G. Di Toro, W. A. Griffith, A. Bistacchi, S. A. Smith, and S. Nielsen  
851 (2012), Inferring earthquake physics and chemistry using an integrated field and  
852 laboratory approach, *J. Struct. Geol.*, 39, 2–36, doi: 10.1016/j.jsg.2012.02.018.

853 Passelègue, F. X., E. Spagnuolo, M. Violay, S. Nielsen, G. Di Toro and A. Schubnel  
854 (2016), Frictional evolution, acoustic emissions activity, and off-fault damage in  
855 simulated faults sheared at seismic slip rates, *J. Geophys. Res.*, 121, 7490–7513,  
856 doi: 10.1002/2016JB012988.

857 Proctor, B.P., Mitchell, T.M., Hirth, G., Goldsby, D., Zorzi, F., Platt, J.D., and Di Toro,  
858 G. (2014), Dynamic weakening of serpentinite gouges and bare surfaces at  
859 seismic slip rates: *Journal of Geophysical Research*, v. 119, doi: 10.1002/  
860 /2014JB011057.

861 Reches, Z., and D. A. Lockner (2010), Fault weakening and earthquake instability by  
862 powder lubrication, *Nature*, 467, 452–455, doi: 10.1038/nature09348.

863 Rice, J. R (2006), Heating and weakening of faults during earthquake slip, *J. Geophys.*  
864 *Res.*, 111, B05311, doi: 10.1029/2005JB004006.

865 Rowe, C., K. Lamothe, M. Rempe, M. Andrews, T. Mitchell, G. Di Toro, J. Clancy  
866 White and S. Aretusini (2019), Earthquake lubrication and healing explained by  
867 amorphous nanosilica, *Nature Communications*, 10, 320, doi:  
868 10.1038/s41467-018-08238-y.

869 Shand, S. J. (1916), The pseudotachylyte of Parys, *Geol. Soc. London Quart. Jour.* 72,  
870 198–221.

871 Shimamoto, T. and H. Nagahama (1992), An argument against the crush origin of  
872 pseudotachylytes based on the analysis of clast-size distribution, *J. Struct. Geol.*,  
873 14, 999–1006, doi: 10.1016/0191-8141(92)90031-Q.

874 Shimamoto, T. and A. Tsutsumi, (1994). A new rotary-shear high-speed frictional  
875 testing machine: Its basic design and scope of research, *J. Tectonic Res. Group of*  
876 *Japan*, 39, 65–78 (in Japanese with English abstract).



877 Sibson, R. H (1975), Generation of pseudotachylyte by ancient seismic faulting.  
878 Geophysical Journal International, 43(3), 775–794, doi:  
879 10.1111/j.1365-246X.1975.tb06195.x.

880 Song, S. R., L. W. Kuo, E. C. Yeh, C. Y. Wang, J. H. Hung, and K. F. Ma (2007a),  
881 Characteristics of the lithology, fault-related rocks and fault zone structures in  
882 the TCDP Hole-A, Terr. Atmos. Ocean. Sci. 18, 243–269, doi:  
883 10.3319/TAO.2007.18.2.243(TCDP).

884 Song, Y. -F., et al. (2007b), X-ray beamlines for structural studies at the NSRRC  
885 superconducting wavelength shifter, J. Synchrotron Radiat. 14, 320–325, doi:  
886 10.1107/S0909049507021516.

887 Spagnuolo, E., Plümper, O., Violay, M., Cavallo, A., Di Toro, G., 2015. Fast-moving  
888 dislocations trigger flash weakening in carbonate-bearing faults during  
889 earthquakes. Sci. Rep.5, 1–11. <https://doi.org/10.1038/srep16112>.

890 Spray, J. G. (1987), Artificial generation of pseudotachylyte using friction welding  
891 apparatus: Simulation of melting on a fault plane, J. Struct. Geol., 9, 49–60, doi:  
892 10.1016/0191-8141(87)90043-5.

893 Spray, J. G. (1992), A physical basis for the frictional melting of some rock-forming  
894 minerals, Tectonophysics, 204, 205–221, doi: 10.1016/0040-1951(92)90308-S.

895 Spray, J. G. (1993), Viscosity determinations of some frictionally generated silicate  
896 melts: Implications for fault zone rheology at high strain rates, J. Geophys. Res.,  
897 v. 98, p. 8053–8068, doi: 10.1029/93JB00020.

898 Spray, J. G. (1995), Pseudotachylyte controversy: fact or friction. Geology, 23, 1119–  
899 1122, doi: 10.1130/0091-7613(1995)023<1119:PCFOF>2.3.CO;2.

900 Spray, J. G. (2005), Evidence for melt lubrication during large earthquakes, Geophys.  
901 Res. Lett., 32, L07301, doi: 10.1029/2004GL022293.

902 Spray, J.G. (2010), Frictional melting processes in planetary materials: from  
903 hyper-velocity impacts to earthquakes. Annu. Rev. Earth Planet. Sci.38, 221–254,  
904 doi: org/10.1146/annurev.earth.031208.100045.

905 Steinike, U. and K. Tkáčová (2000), Mechanochemistry of Solids—Real Structure  
906 and Reactivity, Journal of Materials Synthesis and Processing, 8, 197, doi:  
907 10.1023/A:1011364110355.

908 Tsutsumi, A. and T. Shimamoto (1997), High-velocity frictional properties of gabbro,  
909 Geophys. Res. Lett., 24, 699–702, doi: 10.1029/97GL00503.

910 Tsutsumi, A. (1999), Size distribution of clasts in experimentally produced  
911 pseudotachylytes, J. Struct. Geol., 21, 305–312, doi:  
912 10.1016/S0191-8141(98)00113-8.

913 Violay, M., G. Di Toro, S. Nielsen, B. Gibert, E. Spagnuolo, P. Azais, and P. G.  
914 Scarlato, (2014a), Effect of glass on the frictional behavior of basalts at seismic

915 slip rates, *Geophys. Res. Lett.*, 41, 348–355, doi: 10.1002/2013GL058601.

916 Violay, M., S. Nielsen, B. Gibert, E. Spagnuolo, A. Cavallo, P. Azais, S.  
917 Vinciguerra, and G. Di Toro (2014b), Effect of water on the frictional behavior of  
918 cohesive rocks during earthquakes. *Geology*, 42 (1), 27–30.

919 Violay, M., F. Passelegue, E. Spagnuolo, G. Di Toro and C. Cornelio (2019), Effect of  
920 water and rock composition on re-strengthening of cohesive faults during the  
921 deceleration phase of seismic slip pulses, *Earth and Planetary Sciences*, 522, 55–  
922 64, doi: 10.1016/j.epsl.2019.06.027.

923 Wallace, P. A., S. H. De Angelis, A. J. Hornby, J. E. Kendrick, S. Clesham, F. W. von  
924 Aulock, A. Hughes, J. E. P. Utley, T. Hirose, D. B. Dingwell, and Y. Lavallé  
925 (2019), Frictional melt homogenisation during fault slip: Geochemical, textural  
926 and rheological fingerprints, *Geochimica et Cosmochimica Acta*, 255, 265–288,  
927 doi: 10.1016/j.gca.2019.04.010.

928 Yang, C. H., W.-L. Yu, J.-J. Dong, C.-Y. Kuo, T. Shimamoto, C.-T. Lee, T. Togo, and  
929 Y. Miyamoto (2014), Initiation, movement, and run-out of the giant Tsaoiling  
930 landslide — what can we learn from a simple rigid block model and a velocity–  
931 displacement dependent friction law? *Eng. Geol.*, 182, 158–181, doi:  
932 10.1016/j.enggeo.2014.08.008.

933 Yin, G.-C., Y.-F. Song, M.-T. Tang, F.-R. Chen, K. S. Liang, F. W. Duerwer, M. Feser,  
934 W. Yun and H.-P. D. Shieh (2006), 30 nm resolution X-ray imaging at 8 keV  
935 using third order diffraction of a zone plate lens objective in a transmission  
936 microscope, *Appl. Phys. Lett.*, 89, doi:10.1063/1.2397483.

937

### 938 **Captions**

939 Figure 1. (a) Geological setting of the Hopping area with complex tectonic structures.  
940 The inset box shows the location of the Hopping area in northeast Taiwan. The study  
941 area consists mainly of marble, granitic gneiss, and schist. The Hopping  
942 pseudotachylyte (red star) and its surface structure "brushlines" (green box; the  
943 surface was coated by Pt for SEM analysis) and the Hopping borehole are located  
944 alongside the Hopping River and are hosted in granitic gneiss. The attitude of foliation  
945 is mostly parallel or sub-parallel to the direction of fold axis. (b, c) Specimen  
946 assembly for LHVR and SHIVA. Note that the specimen size for LHVR is 25 mm in  
947 diameter and for SHIVA, the outer diameter is 50 mm and the inner diameter is 30  
948 mm. Specimens were bound with iron wires and jacketed with aluminum rings for  
949 LHVR and SHIVA, respectively.

950

951 Figure 2. Mechanical and compiled data from experiments performed with LHVR and  
952 SHIVA machines. (a) Apparent friction coefficient as a function of displacement

953 under normal stresses from 3 to 30 MPa and slip velocity at 1.3 m/s (LHVR) and 5  
954 m/s (SHIVA) under room humidity (LHVR) and vacuum (SHIVA) conditions. The  
955 static friction, initial weakening, first peak and second peak are indicated by the  
956 arrows. (b) Shear stress of the first peak (red circle), second peak (blue diamond), and  
957 steady-state value (black square) varied with normal stress. Note that the dynamic  
958 shear strength for peak states and steady state is well below Byerlee's friction values  
959 ( $0.6 < \mu < 0.85$ ).

960

961 Figure 3. Evolution of the apparent friction coefficient, slip velocity, axial  
962 displacement and temperature with displacement of five slip-stepping experiments. (A)  
963 State A (LHVR0487) stopped at the peak value representing the first  
964 slip-strengthening behavior. (B) State B (LHVR0534) was stopped at the second  
965 slip-weakening behavior. (C) State C (LHVR0452) stopped at the second  
966 slip-strengthening behavior. (D) State D (LHVR0438) was stopped at the steady-state  
967 value. (E) The experiment reproducing the condition of LHVR0438 with outcrop  
968 sample coupled with the infrared thermal-sensing camera. The temperature increases  
969 with slip from 150°C (minimum detected value of the infrared camera) at the slip of  
970 ~0.4 m to ~850°C ( $\varepsilon = 0.55$ ) and ~600°C ( $\varepsilon = 0.9$ ) at the slip of ~5.3m.

971

972 Figure 4. Experimental results of four states with corresponding schematic sketch of  
973 the solidified frictional melt distribution on the slip surface. The petrographic sections  
974 were prepared to be perpendicular to the slip surface and analyzed from half-way  
975 from the center to the edge. (a–d) Open Nicol observation of the experimental  
976 products. The frictional melt distribution evolves from the melt patches in State A, to  
977 a donut-shape melt layer in State B (5x intensity for compare) and C, to a fully  
978 covered melt layer in State D, respectively. (e) In situ synchrotron XRD analysis of  
979 the host rock and the experimental products from the simulated fault surface. The  
980 disappearance of the diffraction peak of mica and reduction of the diffraction intensity  
981 of feldspar and quartz are reflected in the XRD spectra and show no variation between  
982 the four states. The different colors between the melt spectra are indicated by the  
983 calculated bulk temperature where the red line refers to a higher melting temperature  
984 than the pink lines.

985

986 Figure 5. BSE images of the frictional melts for four states. (a) In State A, quartz  
987 grains (dark grey) with sizes ranging from 2 to 10  $\mu\text{m}$  are abundant within the melt  
988 matrix (light grey). For (b), State B, the number of quartz grains with a size lower  
989 than 5  $\mu\text{m}$  decreased. For (c), State C, smaller quartz grains ( $< 1 \mu\text{m}$ ) appeared while  
990 larger quartz grains ( $> 10 \mu\text{m}$ ) disappeared. For (d), State D, quartz grains with sizes

991 larger than 10  $\mu\text{m}$  are dominant within the melt. The dark area with spherical to  
992 ellipsoidal occurrence are vesicles, which are particularly larger in State D.

993

994 Figure 6. TXM images of the solidified frictional melts for the four states. Internal  
995 microstructures all show substantial ultrafine quartz grains with sub-angular and  
996 angular-to-spherical, and ellipsoidal surrounded by a melt matrix. (a) The enlarged  
997 image highlights the appearance of the fractured grains. (b) The enlarged image  
998 highlights the overlapping occurrence of ultrafine spherical quartz. (c) The enlarged  
999 image shows no distinct boundary of ultrafine quartz with a sub-angular to the  
1000 spherical shape. (d) The enlarged image shows a distinct occurrence of ultrafine  
1001 spherical to ellipsoidal quartz.

1002

1003 Figure 7. Representative Raman spectra of the glass from four states, quartz, and  
1004 water. The signal for the presence of water is barely observed for each state.

1005

1006 Figure 8. Non-Arrhenian temperature dependence of viscosity for four states. The  
1007 viscosity curves were derived using the GRD viscosity model of the Giordano et al.  
1008 (2008) based on the chemical composition of the glass matrix. The apparent viscosity  
1009 corrected with clast content ( $\eta_c$ ) was derived from the mechanical data. Intersection  
1010 points are the estimates of temperature of chemo-mechanical data for the four states.  
1011 The temperatures achieved for states A to C were estimated between the achieved  
1012 temperature of State D and the melting point of muscovite obtained by slow heating  
1013 (650°C) and fast heating rate (900°C) experiments. See the main text for further  
1014 discussion. Two temperatures obtained by infrared measurement from emissivity ( $\epsilon$ )  
1015 of 0.55 and 0.9 were plotted.

1016

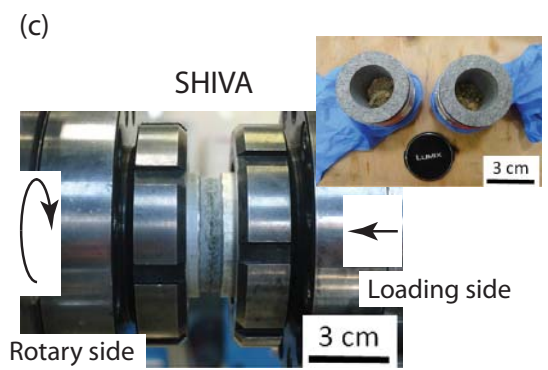
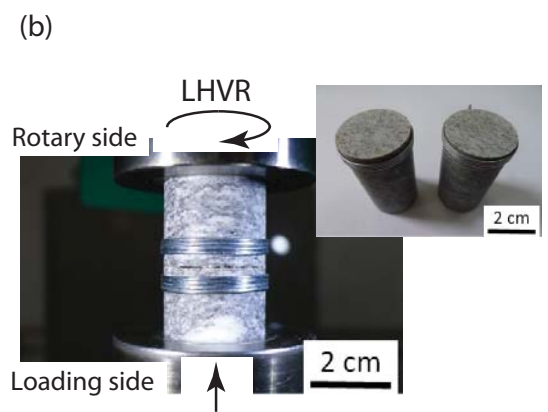
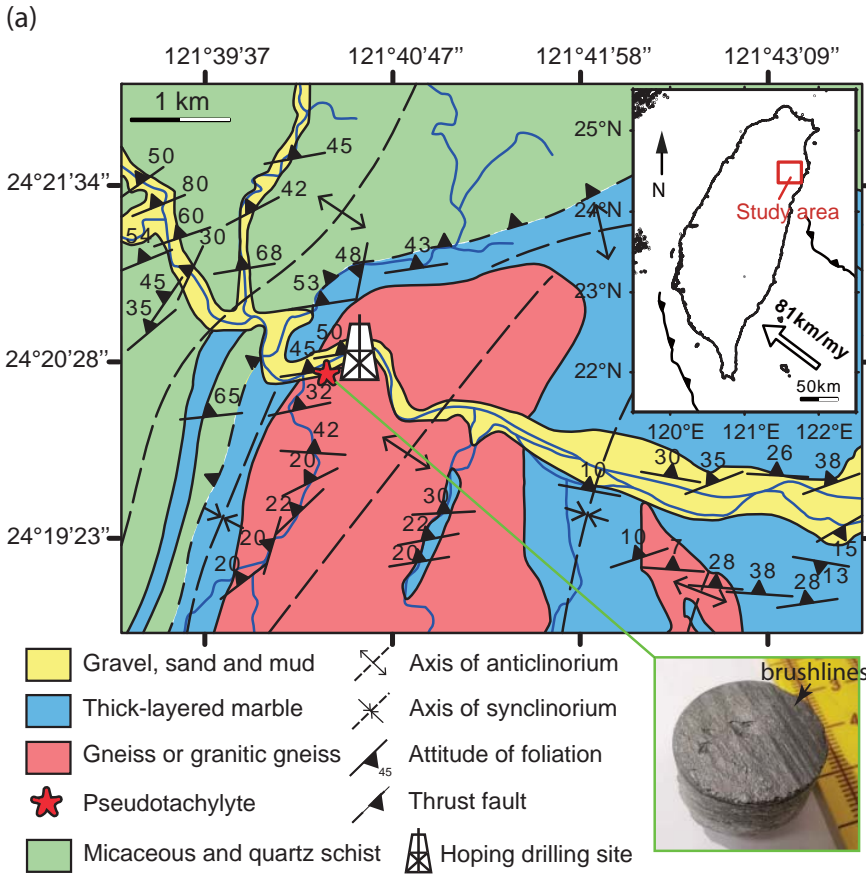
1017 Figure 9. Particle size distribution of surviving grains within the melt matrix for four  
1018 states. Cumulative particle density as a function of mean diameter. The particle  
1019 density,  $N(r)$  representing the cumulative number of particles per  $\mu\text{m}^2$ , following a  
1020 function of particle mean diameter ( $r$ ) in micrometers with regression lines (solid lines)  
1021 in a form of power law  $N(r) = N'(1 + r/r')^{-D}$ . The obtained particle density from TXM  
1022 analyses is relatively higher than the interpolated regression line (dashed line) for the  
1023 four states.

1024

1025 Figure 10. Frictional evolution with displacement for crystalline silicate rocks. (a)  
1026 Schematic sketch of the frictional evolution of Sierra white granite sheared at a slip  
1027 velocity of 0.048 m/s under a normal stress of 1.22 MPa (after Chen et al., 2017b).  
1028 The associated slipping mechanisms corresponding to each stage were shown. (b)

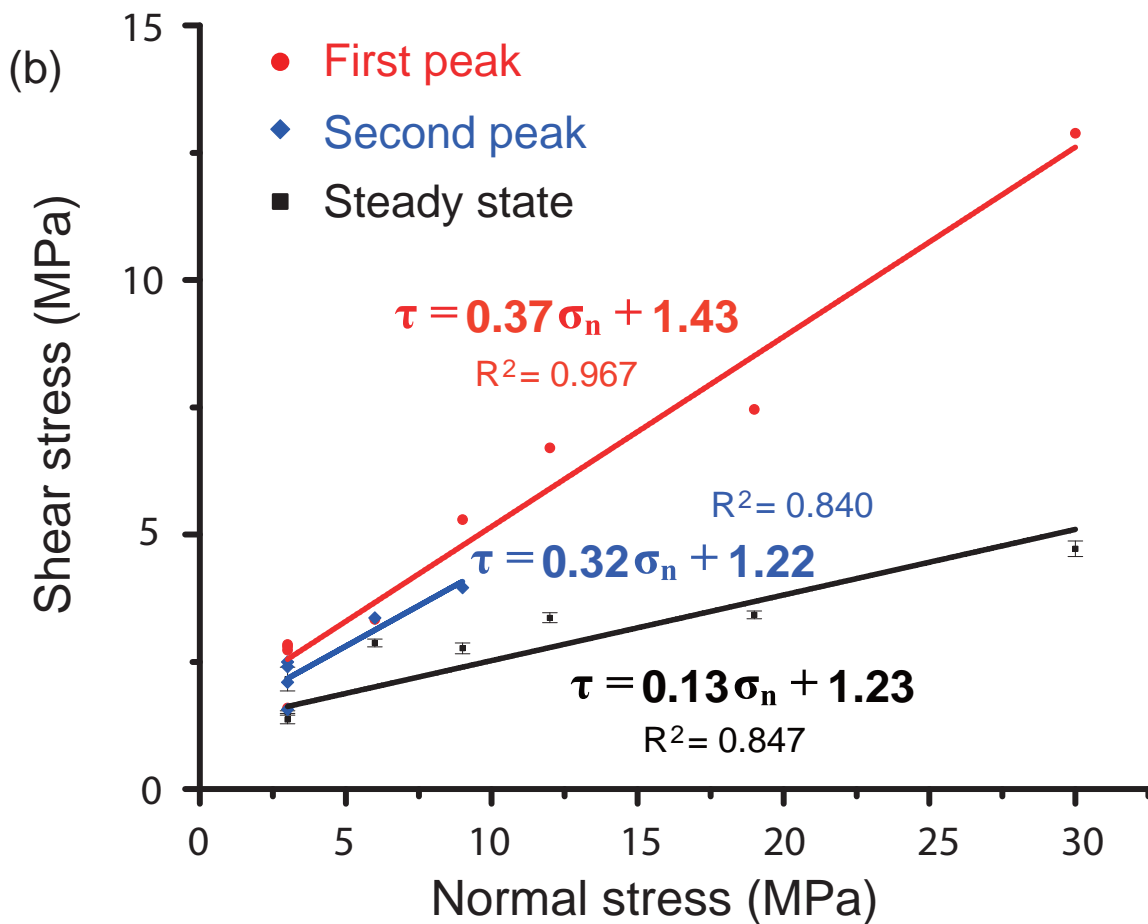
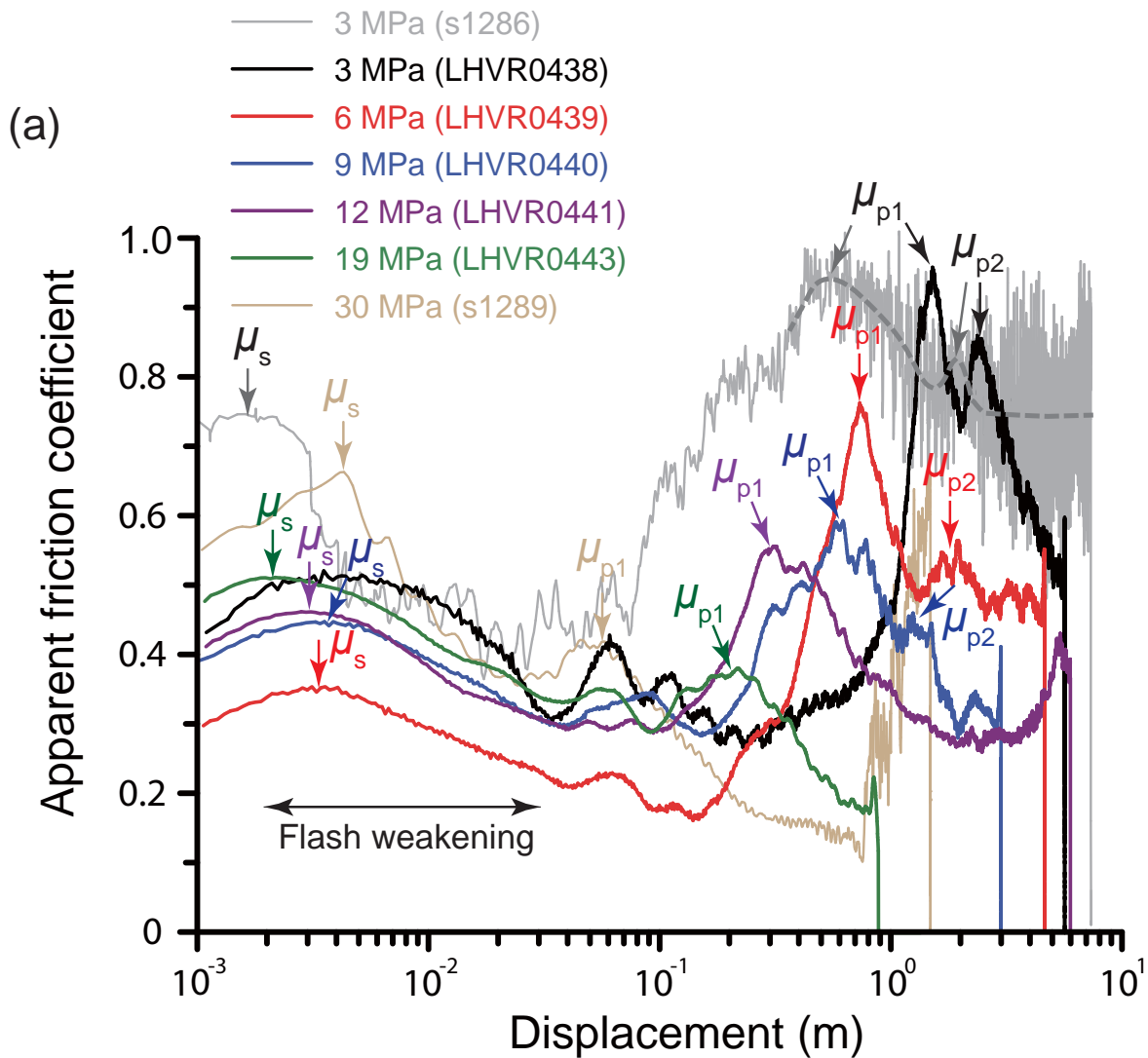
1029 Indian Gabbro sheared at a slip velocity of 0.85 m/s under a normal stress of 1.5 MPa  
1030 (after Hirose and Shimamoto, 2005). (c) South Africa gabbro sheared at a slip velocity  
1031 of 3 m/s under a normal stress of 20 MPa (after Niemeijer et al., 2012). (d) Tonalite  
1032 sheared at a slip velocity of 1.3 m/s under a normal stress of 20 MPa (after Di Toro et  
1033 al., 2006b). (e) Schematic sketch of the frictional evolution of granitic gneiss sheared  
1034 at a slip velocity of 1.3 m/s under a normal stress of 3 MPa. Similar to Chen et al.  
1035 (2017a), the evolution of powder, melt growth, and temperature with displacement is  
1036 further added into our conceptual model and Stage 2 is further delimited into two  
1037 regimes by the grey line. The four schematic diagrams of the slipping zone summarize  
1038 how the PSD, particle volume fraction, melt distribution, microstructures and clast  
1039 packing varied with frictional evolution with slip for the reference experiment  
1040 LHVR0438.

Figure\_01.

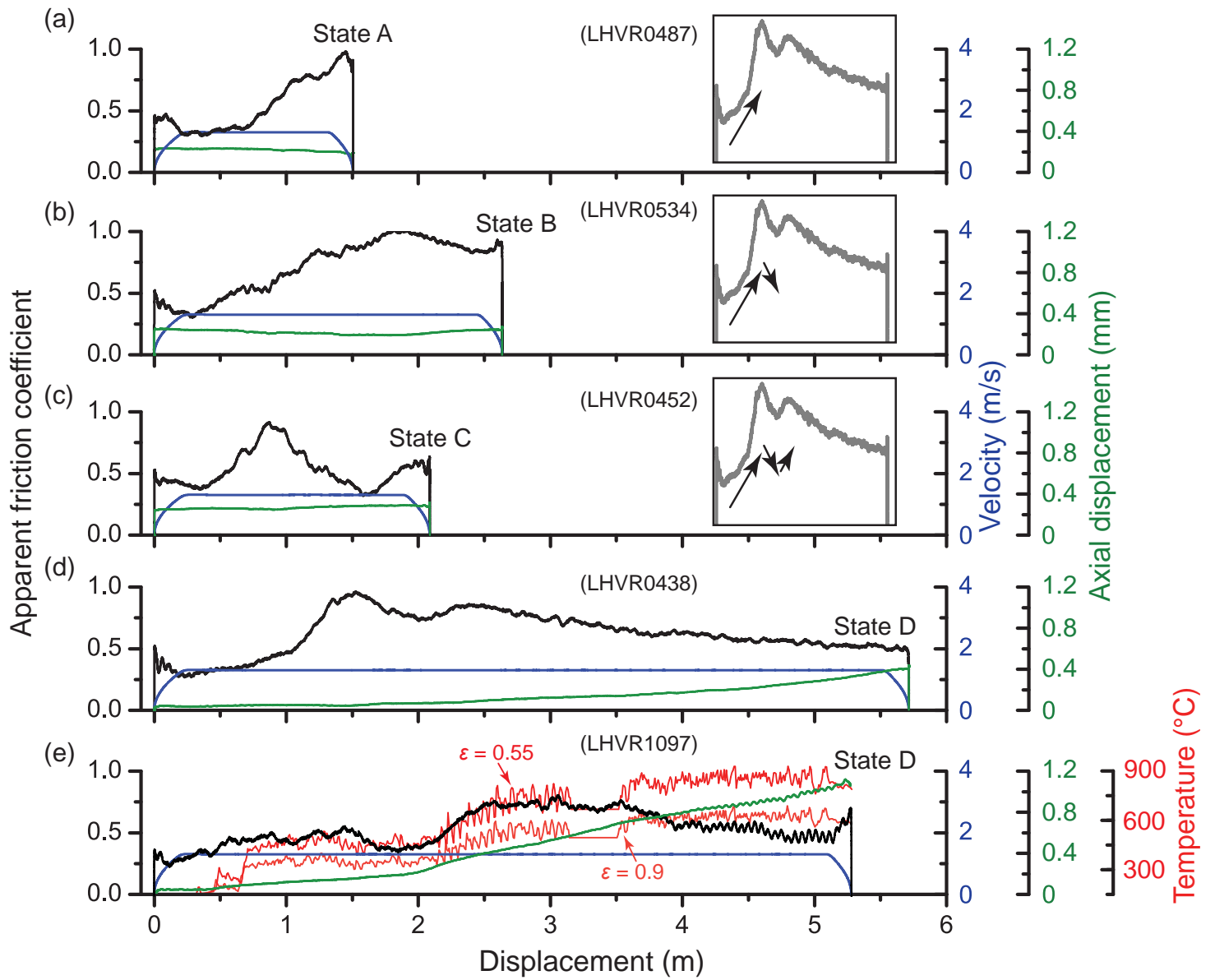


Figure\_02.

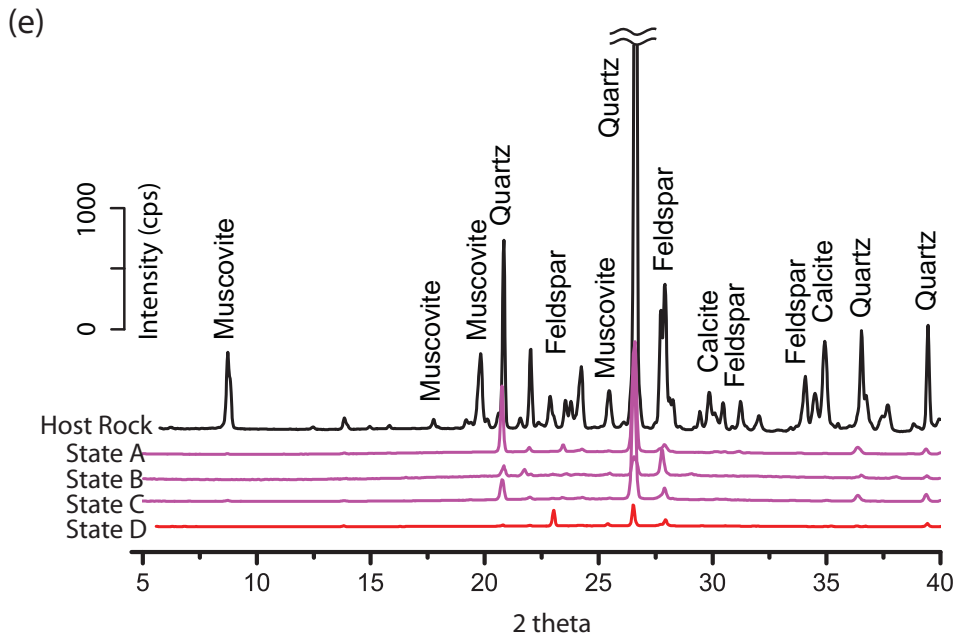
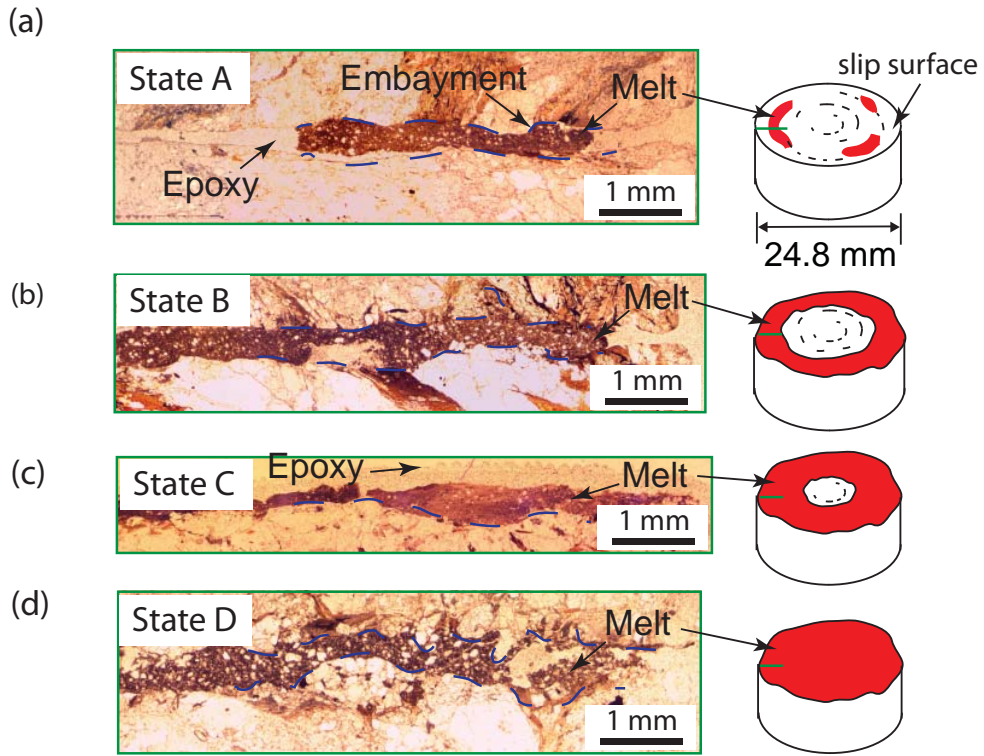




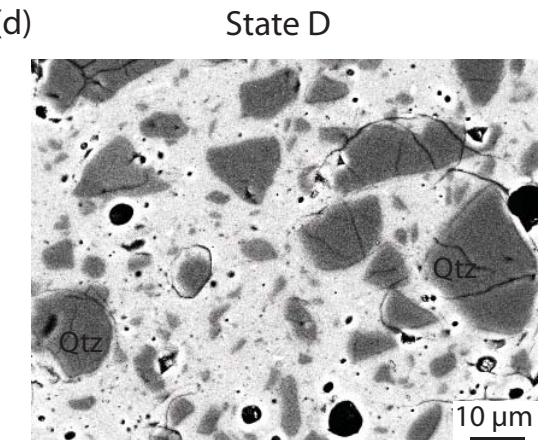
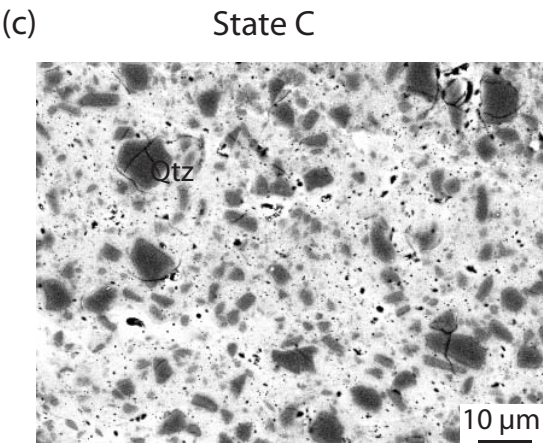
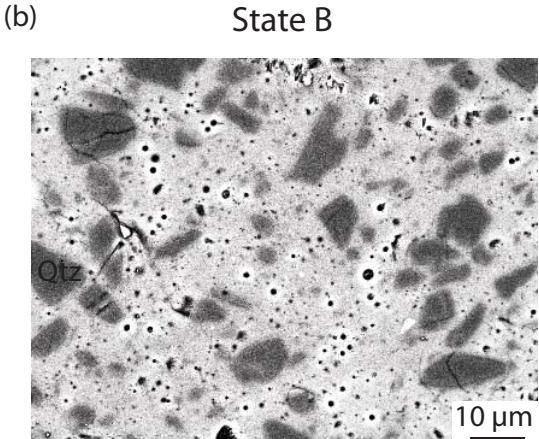
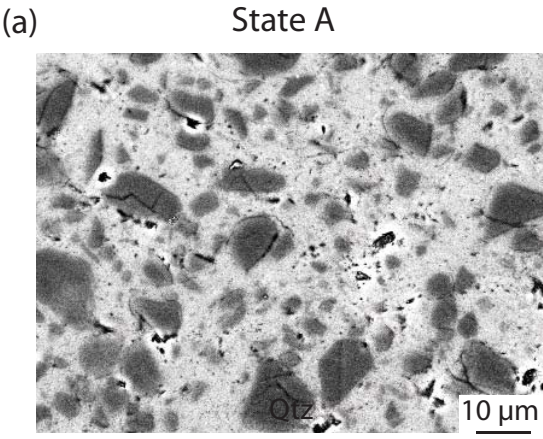
Figure\_03.



Figure\_04.

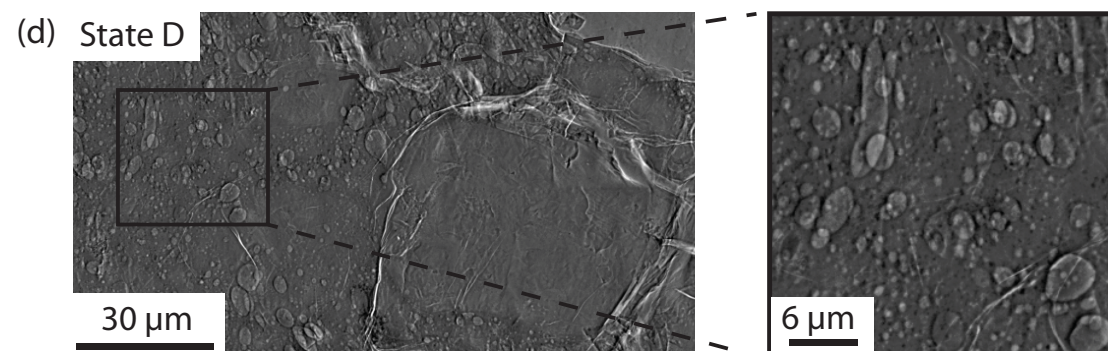
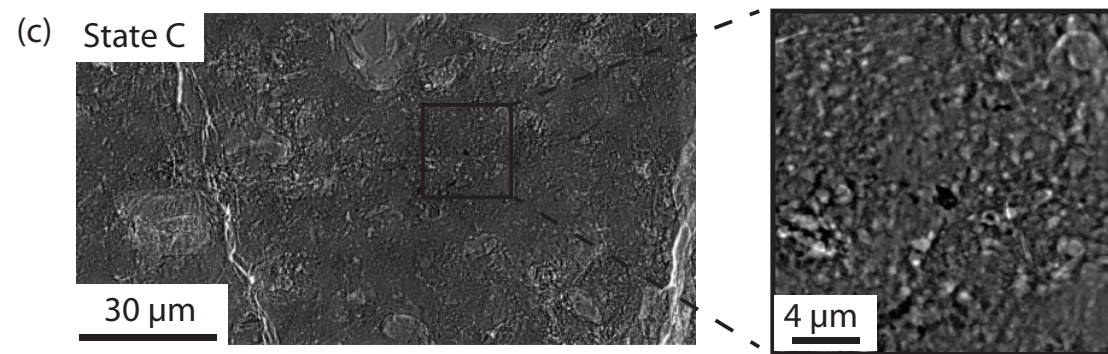
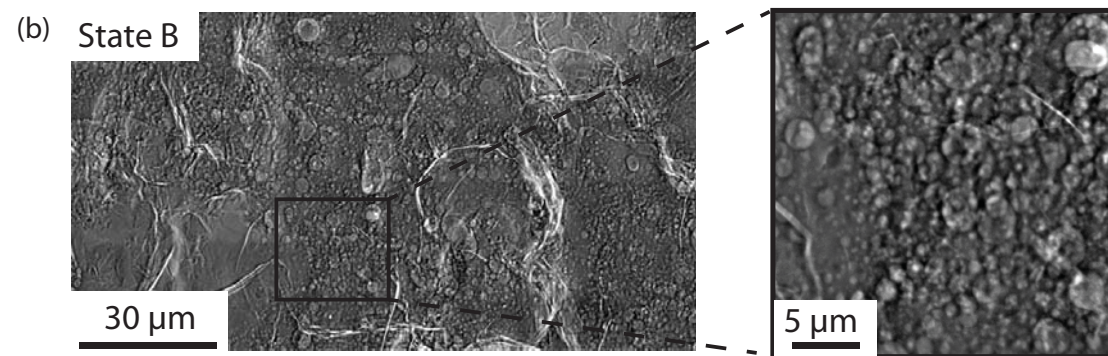
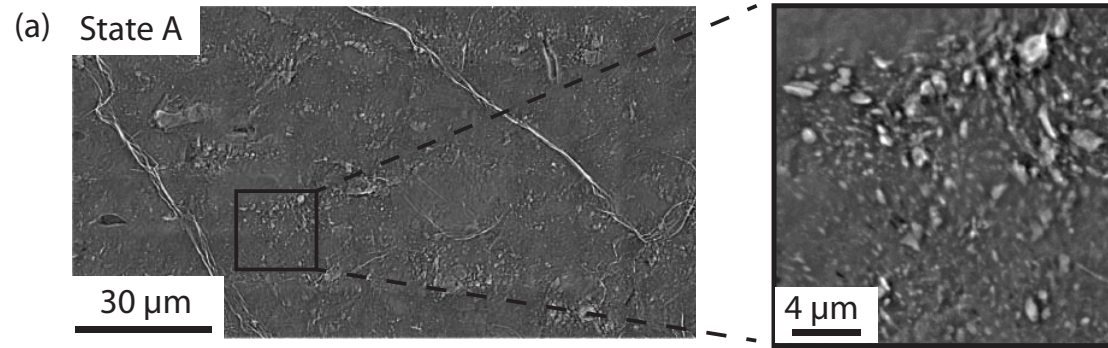


Figure\_05.

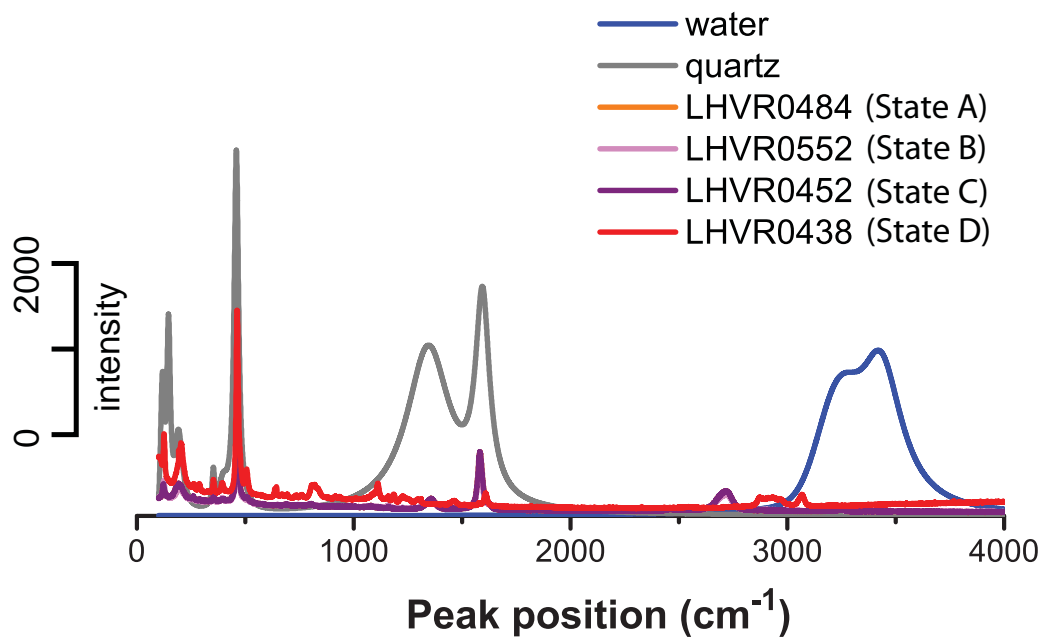


Figure\_06.

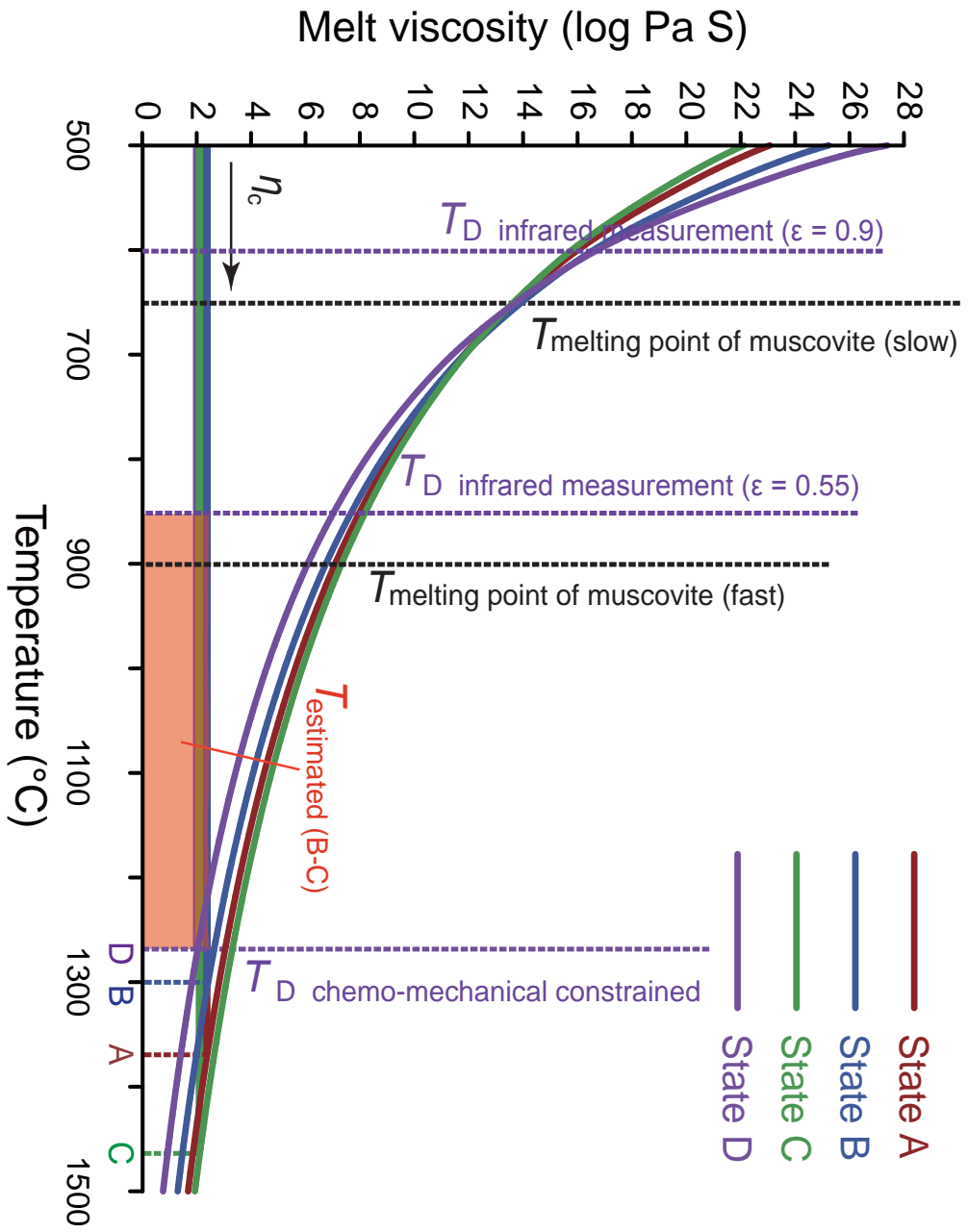




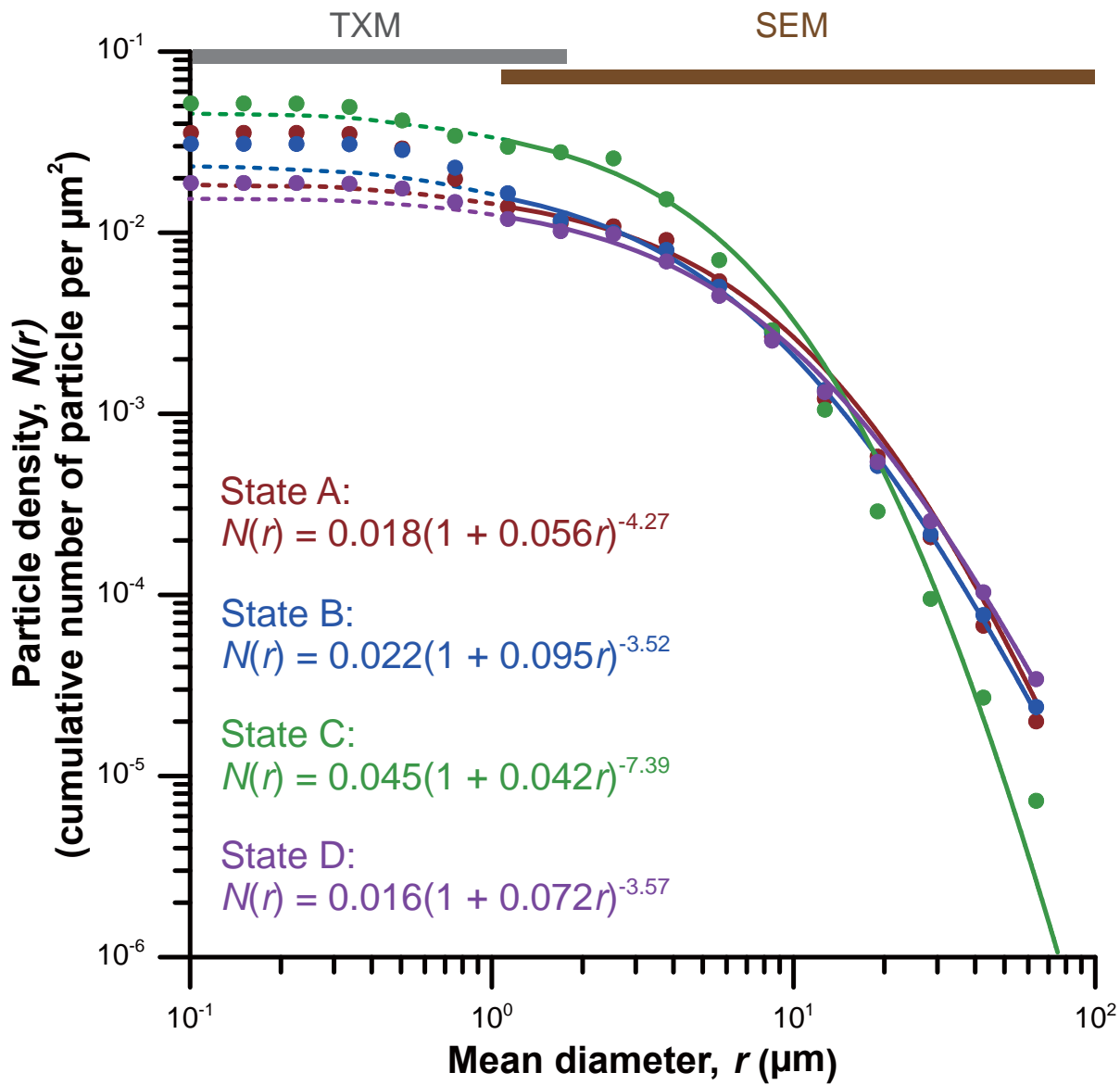
Figure\_07.



Figure\_08.



Figure\_09.



Figure\_01.



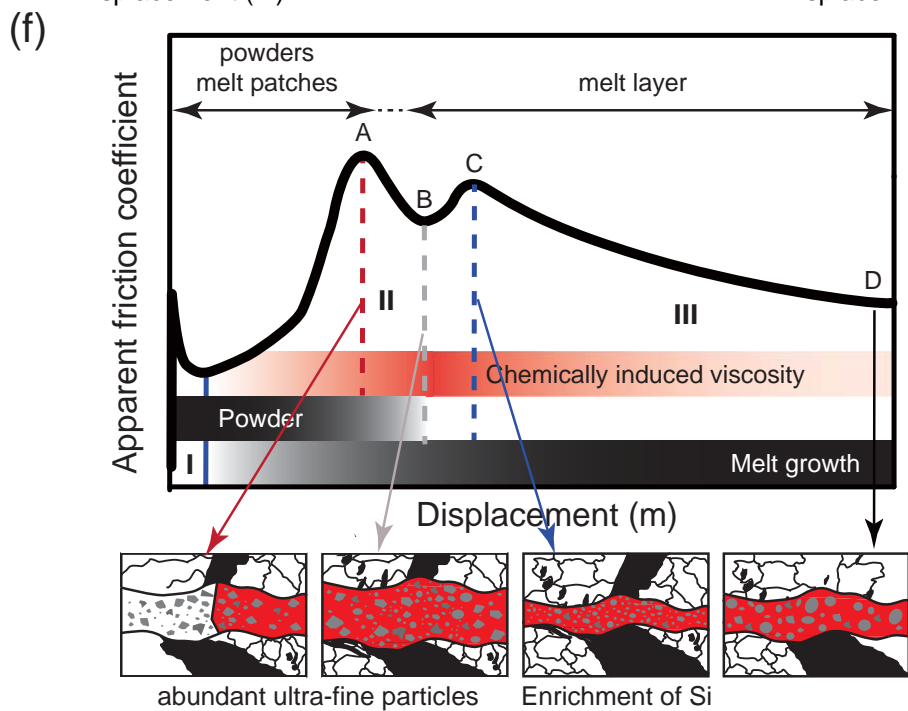
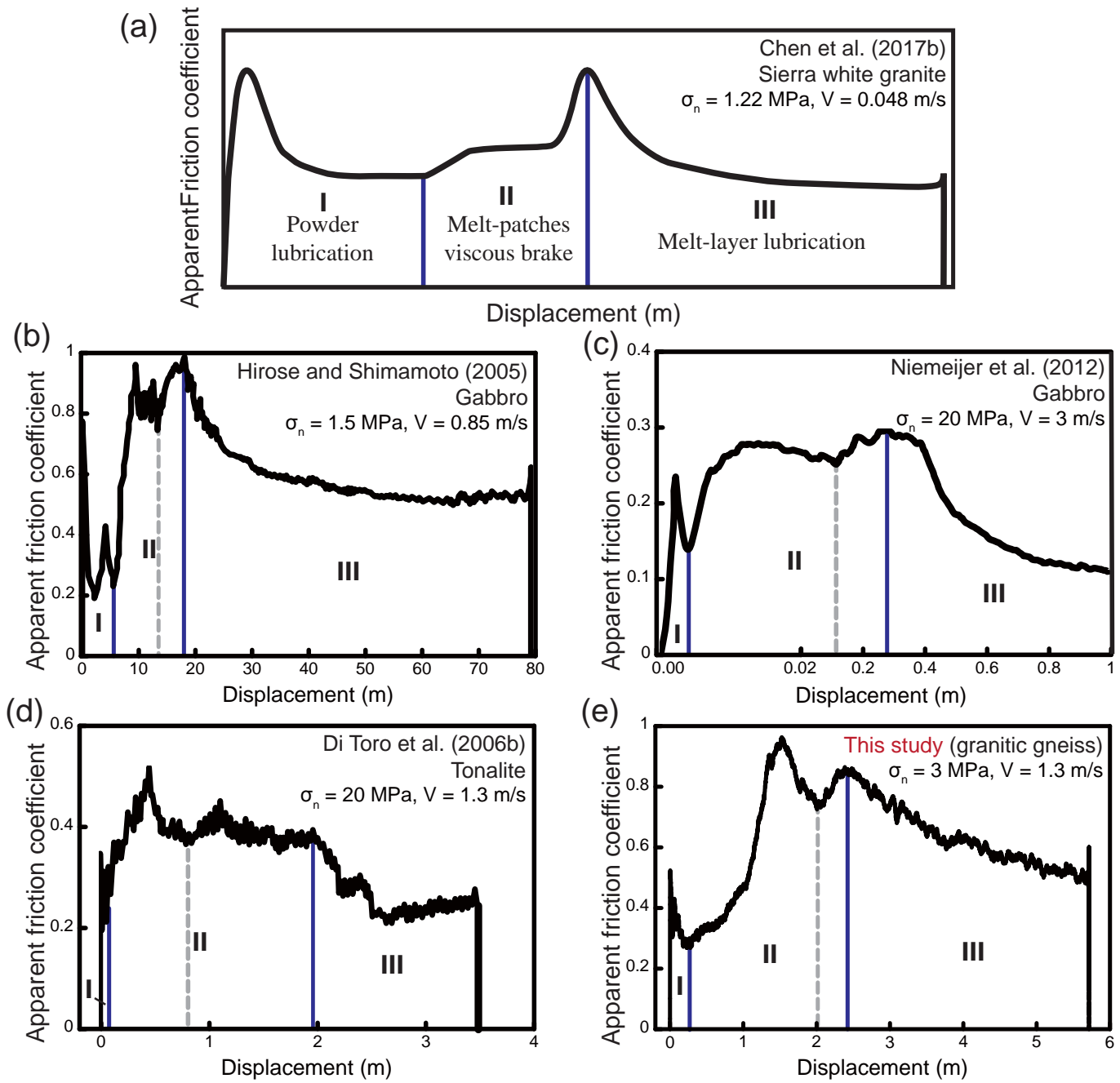


Table 1. Normalized average chemical composition of the granitic gneiss, glass matrix at four states, and chemically-based melt viscosity. *Noted that the bulk composition of the granitic gneiss is cited from Kuo (2016) which using XRF to analyze four rock samples.*

	n	Si	Al	Mg	Ca	Na	K	Ti	Fe	Mn	P	Total	Estimated melt viscosity range (Pa s)
Granitic gneiss (Kuo, 2016)	4	65.6 ± 2.42	16.2 ± 0.67	1.8 ± 0.13	2.8 ± 0.44	2.7 ± 0.05	3.8 ± 0.28	1.0 ± 0.14	5.8 ± 1.21	0.1 ± 0.00	0.2 ± 0.05	100.00	–
State A (LHVR0484)	39	58.3 ± 5.87	18.6 ± 2.64	2.1 ± 0.39	4.2 ± 0.77	2.9 ± 0.51	6.2 ± 0.82	0.6 ± 0.63	7.2 ± 1.25	–	–	100.00	10 <sup>8.0–3.1</sup>
State B (LHVR0552)	40	53.0 ± 3.47	20.4 ± 1.35	2.6 ± 0.46	4.9 ± 1.12	2.7 ± 0.85	7.1 ± 0.63	1.0 ± 0.59	8.4 ± 1.48	–	–	100.00	10 <sup>7.7–2.7</sup>
State C (LHVR0452)	39	61.3 ± 5.91	17.5 ± 2.63	2.2 ± 0.42	4.4 ± 1.22	3.0 ± 0.52	6.1 ± 0.92	0.2 ± 0.39	5.3 ± 1.20	–	–	100.00	10 <sup>8.2–3.3</sup>
State D (LHVR0438)	40	50.1 ± 3.02	17.2 ± 1.54	2.5 ± 0.3	13.5 ± 1.92	2.8 ± 0.31	6.3 ± 0.95	0.6 ± 1.34	7.0 ± 1.62	–	–	100.00	10 <sup>7.1–2.7</sup>

n, number of analyses.

Table 2. List of experiments, experimental conditions, mechanical data, and mechanically-constrained apparent viscosity.

Experiment	$\sigma_n$ (MPa)	First Peak $\tau_{p1}$ (MPa)	Second peak $\tau_{p2}$ (MPa)	Average steady state $\tau_{ss}$ (MPa)	Slip velocity $V$ (m/s)	Total slip $D$ (m)	Acceleration/ Deceleration ( $m/s^2$ )	Melt thickness $w$ (mm)	Apparent viscosity $\eta_{app}$ (Pa S)	Clast content $\phi$ (%)	Apparent viscosity corrected with clasts $\eta_c$ (Pa S)	Ambient condition
LHVR0484 (State A)	3	4.7	–	–	1.3	1.6	3.5	0.27	613	20	229	RH
LHVR0487 (State A)	3	2.9	–	–	1.3	1.5	3.5	–	–	–	–	RH
LHVR0534 (State B)	3	3	–	–	1.3	2.6	3.5	–	–	–	–	RH
LHVR0552 (State B)	3	3	–	–	1.3	2.7	3.5	0.33	548	18	232	RH
LHVR0452 (State C)	3	2.5	1.55	–	1.3	2.1	3.5	0.17	203	11	125	RH
LHVR0438 (State D)	3	2.8	2.5	1.5	1.3	5.7	3.5	0.23	265	20	99	RH
LHVR1097 (State D)	3	1.6	2.1	1.4	1.3	5.3	3.5	–	–	–	–	RH
LHVR0439	6	4.6	3.4	2.8	1.3	4.7	3.5	–	–	–	–	RH
LHVR0440	9	5.3	4	2.8	1.3	3	3.5	–	–	–	–	RH
LHVR0441	12	6.7	–	3.3	1.3	6	3.5	–	–	–	–	RH
LHVR0443	19	7.5	–	3.4	1.3	1.9	3.5	–	–	–	–	RH
s1286	3	3	2.4	1.6	5	7.5	6.5	–	–	–	–	Vacuum
s1289	30	12.7	–	4.7	5	1.5	6.5	–	–	–	–	RH

RH, room humidity